J. Fluid Mech. (2004), *vol.* 512, *pp.* 223–256.
DOI: 10.1017/S0022112004009759 Printed in the United Kingdom

Dynamics and breakup of a contracting liquid filament

By PATRICK K. NOTZ† AND OSMAN A. BASARAN

Department of Chemical Engineering, Purdue University, West Lafayette, IN 47907-1283, USA

(Received 4 June 2002 and in revised form 28 March 2004)

Contraction of a filament of an incompressible Newtonian liquid in a passive ambient fluid is studied computationally to provide insights into the dynamics of satellite drops created during drop formation. This free boundary problem, which is composed of the Navier–Stokes system and the associated initial and boundary conditions that govern the evolution in time of the filament shape and the velocity and pressure fields within it, is solved by the method of lines incorporating the finite element method for spatial discretization. The finite element algorithm developed here utilizes an adaptive elliptic mesh generation technique that is capable of tracking the dynamics of the filament up to the incipience of pinch-off without the use of remeshing. The correctness of the algorithm is verified by demonstrating that its predictions accord with (*a*) previously published results of Basaran (1992) on the analysis of finite-amplitude oscillations of viscous drops, (*b*) simulations of the dynamics of contracting filaments carried out with the well-benchmarked algorithm of Wilkes *et al.* (1999), and (*c*) scaling laws governing interface rupture and transitions that can occur from one scaling law to another as pinch-off is approached. In dimensionless form, just two parameters govern the problem: the dimensionless half-length L_o and the Ohnesorge number Oh which measures the relative importance of viscous force to capillary force. Regions of the parameter space are identified where filaments (*a*) contract to a sphere without breaking into multiple droplets, (*b*) break via the so-called endpinching mechanism where daughter drops pinch-off from the ends of the main filament, and (*c*) break after undergoing a series of complex oscillations. Predictions made with the new algorithm are also compared to those made with a model based on the slender-jet approximation. A region of the parameter space is found where the slender-jet approximation fares poorly, and its cause is elucidated by examination of the vorticity dynamics and flow fields within contracting filaments.

1. Introduction

Many industrial processes such as gene chip arraying (Schena *et al.* 1998), inkjet printing (Döring 1982) and catalyst production (Shah, Kevrekidis & Benziger 1999) rely on the formation of drops of liquid from a nozzle in air. In nearly all applications involving drop formation, a uniform drop size distribution is desired. However, such a distribution is commonly prohibited by the presence of small secondary or *satellite* drops, which are hereafter referred to as satellites, that are remnants of the drop pinch-off process. Shortly before the primary drop pinches off, a thin thread of liquid connects the forming drop to the liquid remaining in the nozzle. Under some operating

† Present address: Sandia National Laboratory, Albuquerque, NM 87185-0834, USA

conditions, the thread pinches at both ends before it can be absorbed into either the primary drop or the liquid in the nozzle and thus forms a satellite (Zhang & Basaran 1995). In situations where one cannot prevent the formation of satellites, one would like to know whether the satellites will, in time, break up into multiple subsatellites and if so what will be the relative sizes of the subsatellites. A goal of this paper is to provide insights into this problem through the study of the dynamics of the prototypical satellite – a free liquid filament whose initial shape is that of a cylinder with hemispherical caps at both of its ends (see, e.g., Schulkes 1996).

Several researchers have investigated the problem of drop formation experimentally. For more than 50 years, the pioneering studies of Hauser *et al.* (1936) and Edgerton, Hauser & Tucker (1937) have remained among the most illuminating observations of drops and their satellites during drop formation from a nozzle. These authors used a high-speed motion camera at rates up to 1200 frames per second (f.p.s.) to visualize both primary drops and satellites in their study of the drop weight method for surface tension measurement. These authors were primarily interested in determining the number of satellites that form and hence did not focus their observations onto the dynamics of individual satellite drops. Moreover, the frame rates that they were able to achieve, while remarkable in that era, were insufficient for monitoring in detail the time evolution of a single satellite. More than 50 years later, Peregrine, Shoker & Symon (1990) reinvigorated the subjects of drop formation and interface rupture with their photographs of the dynamics shortly before and after the pinch-off of both the primary drops and satellites for water dripping from a capillary (see also Goedde & Yuen 1970; Kowalewski 1996, for related studies of satellite dynamics occurring during breakup of a liquid jet). However, Peregrine *et al.* (1990) only reported the shapes of satellites during the early stages of their evolution. Furthermore, pictures depicting the time evolution of the dynamics reported by these authors were not of the same drop but were of different drops at different stages of their dynamics. Consequently, they were only able to estimate the relative times of their photographs.

Zhang & Basaran (1995) used high-speed visualization to study the effects of physical properties, flow rate, tube radius, tube wall thickness and the presence of surfactants on the primary drop volume, limiting drop length at breakup, and the fate of satellites for drops of glycerol/water solutions forming from a capillary tube. However, they were not able to study the details of the satellite dynamics due to the insufficient time resolution of their imaging system. Shi, Brenner & Nagel (1994) uncovered the fascinating effect of increasing drop viscosity on the shape of a drop near the point of pinch-off. These authors showed that for concentrated glycerol/water solutions, a microthread, or possibly a series of microthreads such that each succeeding microthread was significantly thinner than the one from which it was spawned, could form where the main thread connects to the about-to-form primary drop. Henderson, Pritchard & Smolka (1997) experimentally studied both the pinch-off of the primary drop from the main thread and the pinch-off of the main thread from the fluid pendant from the capillary tube for highly viscous liquids. These authors noted that while one or more microthreads form where the main thread connects to the primary drop, no microthreads form where the main thread connects to the fluid in the capillary. Henderson *et al.* (1997) also compared the recoil speed of the main filament after it separated from either the primary drop or from the fluid in the capillary to that predicted by scaling analysis.

Brenner *et al.* (1997) studied the breakup of water drops and focused primarily on the dynamics for times approaching and after breakup. Although these authors studied the formation of satellites, they only focused on the early stages of the

satellite's dynamics. Recently, Notz, Chen & Basaran (2001) utilized an ultra-high-speed imaging system to uncover the surprising dynamics of a satellite formed during the pinch-off of a water drop from a tube. These authors also illustrated the breakup and re-coalescence of a subsatellite with the satellite. Rothert, Richter & Rehbert (2001) and Chen, Notz & Basaran (2002) showed experimentally the change of scaling from one scaling regime to another (cf. Lister & Stone 1998) as pinch-off nears. Robinson & Steen (2001) and Chen *et al.* (2002) further showed experimentally that a fluid interface can overturn prior to pinch-off even in the presence of finite viscosity by demonstrating its occurrence during breakup of a bridge of a soap film and that of a drop, respectively.

The problem of drop formation has also been the subject of numerous theoretical studies. Schulkes (1994) used the boundary element method (BEM) to solve for the potential flow inside a growing drop to theoretically predict the dynamics of formation and breakup of drops of an inviscid liquid from a capillary. Among other things, Schulkes (1994) showed that the interface of the primary drop at the incipience of breakup is overturned near the pinch-point. Eggers & Dupont (1994) studied the breakup of liquid drops by solving the one-dimensional slender-jet equations (Eggers 1993). These authors also investigated the asymptotic behaviour of interfacial rupture for low-viscosity fluids and contrasted their results with those for an inviscid fluid. Shi *et al.* (1994) solved the one-dimensional equations to predict the cascade of microthreads that form for concentrated glycerol/water solutions shortly before the primary drop detaches from the main thread. These authors showed that while one microthread forms naturally, an external source of noise is necessary to trigger the formation of subsequent microthreads. Brenner *et al.* (1997) studied the formation and pinch-off of low viscosity drops by solving the one-dimensional equations. These authors paid particular attention to the dynamics shortly before and after the point of rupture. Zhang & Stone (1997) used the BEM to theoretically study the formation of drops in Stokes flow into a viscous ambient fluid also undergoing Stokes flow. Among other things, these authors illustrated that the length of the drops at breakup increases significantly while the primary drop volume varies only slightly as the ratio of the drop's viscosity to the external fluid's viscosity increases.

Wilkes, Phillips & Basaran (1999) studied the formation and pinch-off of Newtonian liquid drops from a tube using a three-dimensional axisymmetric or two-dimensional algorithm employing the Galerkin finite element method (G/FEM). These authors demonstrated the high-accuracy of their computations by showing that their computed results (i) agreed with new and old experimental measurements within an error of about a percent and (ii) were in excellent agreement with results obtained with an inviscid code when viscous force was small compared to inertial force. These authors further showed for the first time that the interface of a drop of a liquid of finite viscosity can overturn prior to breakup (cf. Chen *et al.* 2002). Before this work, interface overturning prior to pinch-off had been thought to occur only in the absence of viscosity as the phenomenon had only been observed in inviscid flows (Mansour & Lundgren 1990; Schulkes 1993, 1994; Chen & Steen 1997; Day, Hinch & Lister 1998).

Recently, Zhang (1999) used the volume-of-fluid (VOF) method to predict the formation of several drops of liquid in sequence into air. Among his findings, Zhang reported a correlation for the critical flow rate above which satellites do not form as a function of fluid properties. Gueyffier *et al.* (1999) used a fully three-dimensional VOF algorithm to predict the dynamics of drop formation including the dynamics and formation of satellites. However, the calculations by both Zhang (1999) and Gueyffier

et al. (1999) for the drop shape at the incipience of breakup and subsequent satellite dynamics were too coarse and hence did not capture well the fine details of existing experimental observations (Zhang & Basaran 1995; Notz *et al.* 2001). By contrast, using a finite element algorithm, Chen *et al.* (2002) showed a change of scaling from one scaling regime to another (cf. Lister & Stone 1998) as pinch-off nears. Chen *et al.* (2002) further showed for the first time that the computed value of the minimum neck radius of a forming drop follows Eggers's (1993) so-called universal solution until it becomes unstable. Ambravaneswaran, Wilkes & Basaran (2002) recently compared the predictions of drop formation based on the one-dimensional equations with those based on the full three-dimensional axisymmetric Navier–Stokes equations in order to determine the accuracy of the one-dimensional method under different operating conditions. As part of the same study, these authors used the one-dimensional method to show that if the fluid and tube radius are fixed but the flow rate is varied, there exists a critical flow rate beyond which satellites no longer form. Fuchikami, Ishioka & Kiyono (1999) and Ambravaneswaran, Phillips & Basaran (2000) have also used the one-dimensional equations and experiments to explore the dynamics of the so-called leaky faucet problem and thereby determined computationally and verified experimentally in some situations a number of interesting nonlinear dynamical phenomena including period doubling, hysteresis and chaotic dripping.

Compared to the number of theoretical studies aimed at understanding the dynamics of the formation and pinch-off of drops from a tube, relatively few studies have focused on satellite dynamics to the same level of detail. Schulkes (1996) studied the contraction of liquid filaments in air at finite Reynolds number using the G/FEM. Schulkes took the initial drop shape to be that of a cylinder terminated at both ends by identical hemispherical caps and the fluid to be initially quiescent. Unfortunately, his calculations failed to converge before the interface overturned and/or the minimum radius of the thread was about 80% of the initial thread radius. Notz *et al.* (2001) used the G/FEM to predict the recoil dynamics of an initially quiescent, carrot-shaped filament of liquid in air and showed that this simple prototype satellite exhibits dynamics which closely resemble those of real satellite drops. Furthermore, these authors demonstrated the accuracy of their algorithm by predicting the transition from one scaling law governing interface rupture to another.

In a series of papers, Stone and coworkers (Stone, Bentley & Leal 1986; Stone & Leal 1989; Tjahjadi, Stone & Ottino 1992) studied the breakup of viscous filaments in a viscous surrounding liquid both theoretically, using the BEM, and experimentally. In these works, initially spherical drops of radius a were stretched using an externally applied steady linear flow. These authors studied two situations. In the first, the drops were stretched to a length L, the external flow was stopped, and the drops were allowed to contract under the action of surface tension. In the second situation, the external flow remained on and the filaments were stretched until they broke into two or more drops. In these studies, the main parameters governing the dynamics were the viscosity ratio $\lambda = \hat{\mu}/\mu$, where $\hat{\mu}$ and μ are the viscosity of the droplet and the external fluid, and the capillary number $Ca = \mu G a/\gamma$, where G is the applied shear rate and γ is the interfacial tension. In all of these studies, the Reynolds number $Re = \rho G a^2/\mu$, where ρ is the density of the external fluid, was vanishingly small so these analyses only apply in the Stokes flow or the creeping flow limit.

Of particular interest here are Stone and coworkers' results for situations in which the drop underwent breakup during the relaxation portion of the flow, namely after the external flow was stopped. Among other things, these authors determined the critical dimensionless stretching length L_c/a as a function of λ below which the drops

tended to a sphere at long times and above which the drops broke up into one or more satellites as they contracted. It was shown that L_c/a has a minimum near $\lambda \approx 1$. For $\lambda > O(1)$ ($\lambda < O(1)$), the drops must be stretched to larger L/a to produce breakup because more time is required for the bulbous ends to form and pinch-off to occur due to the stabilizing influence of the viscosity of the inner (outer) fluid.

When a liquid drop or a filament ruptures, the shapes of the interfaces on either side of the pinch point are locally cones (Eggers 1997). Similarly, when a liquid sheet breaks, two wedges of liquid result. In a pioneering study, Keller & Miksis (1983) analysed the recoil of a wedge of an inviscid fluid undergoing irrotational flow. These authors thereby deduced that the ensuing motion is self-similar, with length scales varying as the 2/3 power of time measured from the start of the recoiling. More recently, Billingham (1999) studied theoretically the recoil of both a wedge and a cone accounting for viscous effects. Since both experiment and theory (Eggers 1997; Notz *et al.* 2001) show that in many cases the retracting edge of filaments, wedges, and cones roll up, Keller, King & Ting (1995) carried out an asymptotic analysis to determine the shape of and the flow within an inviscid blob undergoing irrotational flow. Asymptotic expansions valid within the blob could then be matched to ones valid within the rest of a sheet or filament.

Therefore, a comprehensive theoretical understanding of the dynamics of the contraction and breakup of highly stretched liquid filaments in a dynamically inactive ambient fluid, e.g. air, is lacking. Remedying this situation is a major goal of this paper. The remainder of the paper is organized as follows. Section 2 defines in detail the problem under investigation. This section also presents the equations, initial conditions, and boundary conditions that govern the problem. Section 3 describes the numerical algorithm developed to solve the governing equations. Section 4 presents the results of the study. Conclusions and future goals are the subjects of § 5.

2. Problem statement and governing equations

The system is a drop of an isothermal incompressible Newtonian liquid with constant viscosity μ, density ρ and surface tension γ, hereafter called a filament, that is surrounded by a dynamically inactive ambient fluid. Experiments on drop formation from capillaries (Hauser *et al.* 1936; Peregrine *et al.* 1990; Zhang & Basaran 1995; Brenner *et al.* 1997; Henderson *et al.* 1997) and jet breakup (Goedde & Yuen 1970; Kowalewski 1996) have shown that when satellites form, their initial shapes are nearly symmetrical filaments about their equatorial midplanes for high-viscosity liquids but are asymmetrical and cone-like for low-viscosity liquids. However, if a solid surface on which a liquid drop is placed is oscillated to eject a portion of the drop (Wilkes & Basaran 2001; James *et al.* 2003) or drops are generated from a drop-on-demand inkjet nozzle (Döring 1982; Chen & Basaran 2002), symmetrical filaments can be produced for liquids of arbitrary viscosity. Thus, following Schulkes (1996), the initial shape of the filament is taken to be that of an axisymmetric cylinder that is terminated by hemispherical caps at both ends and the fluid within the filament is initially taken to be at rest, i.e. the fluid velocity $\tilde{\boldsymbol{v}} = \boldsymbol{0}$ at time $\tilde{t} = 0$. The initial shape has a dimensional half-length of $\tilde{L}_o$ and radius R and the hemispherical caps at both ends have radii R. Figure 1 schematically illustrates the initial state of the filament. Here, $(\tilde{r}, \theta, \tilde{z})$ are the dimensional radial, azimuthal and axial coordinates of a cylindrical coordinate system which is based at the centre of mass of the filament and, unless otherwise indicated, $\boldsymbol{n}$ and $\boldsymbol{t}$ are the unit outward-normal and tangent vectors to the filament surface.

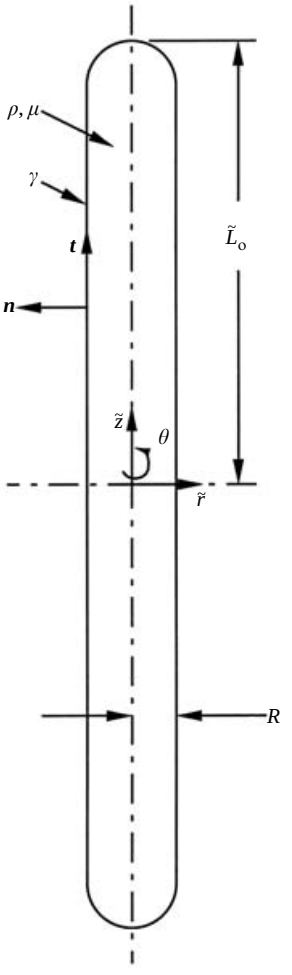

FIGURE 1. Definition sketch for a contracting filament.

Here and in what follows, all variables are non-dimensionalized using the length scale $\ell_c = R$ and the capillary time scale $t_c = \sqrt{\rho R^3/\gamma}$, and quantities denoted with a tilde are the dimensional counterparts of those without. The dynamics of the filament are governed by the dimensionless Navier–Stokes and continuity equations

$$\frac{\partial \boldsymbol{v}}{\partial t} + \boldsymbol{v} \cdot \nabla \boldsymbol{v} = Oh \nabla \cdot \boldsymbol{T}, \tag{2.1a}$$

$$\nabla \cdot \boldsymbol{v} = 0. \tag{2.1b}$$

Here $\boldsymbol{T} = -p\boldsymbol{I} + \nabla \boldsymbol{v} + (\nabla \boldsymbol{v})^T$, where p is pressure, $\boldsymbol{T}$ is the Newtonian stress tensor and the Ohnesorge number, $Oh = \mu/\sqrt{\rho R \gamma}$, measures the relative importance of viscous force to surface tension force. When the characteristic velocity is taken to be $v_c = \ell_c/t_c$, Oh can be interpreted as the reciprocal of the Reynolds number, namely $Re \equiv Oh^{-1}$.

Because the filament is axisymmetric about the z-axis, $r = 0$, and its shape is taken to remain symmetric about the equatorial midplane, $z = 0$, the following boundary

conditions apply along the axis of symmetry $r=0$ and the plane $z=0$:

$$\boldsymbol{n}\cdot\boldsymbol{T}\cdot\boldsymbol{t}=0, \tag{2.2a}$$

$$\boldsymbol{n}\cdot\boldsymbol{v}=0, \tag{2.2b}$$

where $\boldsymbol{n}$ and $\boldsymbol{t}$ stand for the unit normal and tangent vectors to those boundaries. Along the free surface, the shear stress equals zero and the normal stress is proportional to the curvature. Furthermore, the free surface moves according to the kinematic boundary condition. These two conditions are of course the traction and the kinematic boundary conditions:

$$\boldsymbol{n}\cdot\boldsymbol{T}=\frac{1}{Oh}2\mathscr{H}\boldsymbol{n}, \tag{2.3a}$$

$$\boldsymbol{n}\cdot\boldsymbol{v}=\boldsymbol{n}\cdot\dot{\boldsymbol{x}}_s. \tag{2.3b}$$

Here, $-\mathscr{H}$ is the mean curvature of the interface and $\dot{\boldsymbol{x}}_s$ denotes the velocity of points on the free surface located by the position vector $\boldsymbol{x}_s$.

The dynamics is governed by just two dimensionless groups: the dimensionless initial aspect ratio $L_o=\tilde{L}_o/R$ and the Ohnesorge number Oh. The drop volume $V=\tilde{V}/R^3$ is given simply by

$$V=2\pi\left(L_o-\tfrac{1}{3}\right). \tag{2.4}$$

In lieu of the non-dimensionalization given above one could choose as the characteristic length scale the radius a of a sphere with the same volume as the filament. In this alternative formulation the dimensionless groups are $Oh^*=\mu/(\rho\gamma a)^{1/2}$ and either R/a or $L_o^*=\tilde{L}_o/a$. If one chooses Oh^* and R/a, L_o^* is then given by

$$L_o^*=\frac{2/3}{(R/a)^2}+\frac{1}{3}\left(\frac{R}{a}\right). \tag{2.5}$$

Conversely, if one chooses to use Oh^* and L_o^*, R/a must then be found by solving the cubic equation

$$\left(\frac{R}{a}\right)^3-3L_o^*\left(\frac{R}{a}\right)^2+2=0. \tag{2.6}$$

Either way, with the choice of a as the characteristic length scale, all filaments enclose the same volume, $V^*=\tilde{V}/a^3=4\pi/3$. However, $L_o=\tilde{L}_o/R$ is the true initial aspect ratio of the filament whereas R/a and $\tilde{L}_o/a$ are physically less meaningful by themselves. Moreover, the length scale R properly characterizes the curvature of the filament's tips which, in turn, characterizes the driving force of the flow within the contracting filament.

Naturally, the two choices for non-dimensionalization are related. It is straightforward to show that

$$\frac{a}{R}=\left(\tfrac{3}{2}L_o-\tfrac{1}{2}\right)^{1/3} \tag{2.7}$$

and

$$Oh=Oh^*\sqrt{\frac{a}{R}}. \tag{2.8}$$

3. Finite element analysis

Equations (2.1) subject to boundary conditions (2.2) and (2.3) and initial conditions stated in § 2 are solved using the method of lines with the Galerkin/finite element method (Strang & Fix 1973) for spatial discretization and an adaptive finite difference method (Gresho, Lee & Sani 1980) for time integration. Mixed interpolation (Huyakorn *et al.* 1978) is used in representing the velocity and the pressure such that the velocity components are expanded in a set of C^0 biquadratic basis functions and the pressure is expanded in a set of C^0 bilinear basis functions (see e.g. Wilkes *et al.* 1999). With these expansions in place, weighted residuals of the governing equations are formed by using the finite element basis functions as weighting functions and integrating the residual equations over the entire domain A. In order to carry out the integrations of the weighted residual, or weak, form of the governing equations, the domain is first subdivided into a discrete set of smaller subdomains, or elements, referred to as the mesh. Integrations are performed element-by-element by mapping each element from the physical domain onto the standard unit square in the computational domain (Strang & Fix 1973) where they are carried out numerically by Gaussian quadrature. In the following section, the domain discretization method used here is described. In § 3.2 other key aspects of the numerical algorithm, including the method of time integration and an iterative method for solving the resulting system of nonlinear algebraic equations, are outlined. Finally, several tests that verify the accuracy of the current algorithm are presented in § 3.3.

3.1. *Elliptic mesh generation*

For problems involving moving boundaries, the mesh must be able to move and deform. Numerous methods have been developed to enable finite element meshes to deform automatically, including the method of spines (Kistler & Scriven 1983, 1994), pseudo-solid domain deformation (Sackinger, Schunk & Rao 1996), arbitrary Lagrangian–Eulerian (ALE) methods (Hughes, Liu & Zimmermann 1981) and elliptic mesh generation (Ryskin & Leal 1983; Brackbill 1993).

In this paper, the elliptic mesh generation method developed by Christodoulou & Scriven (1992) is used. Their method consists of constructing a weighted combination of functionals which impose orthogonality of coordinate lines, smoothness of coordinate lines and a controlled distribution of elements (see e.g. Knupp & Steinberg 1993). Weighted residuals of the mesh equations are used to determine the unknown mesh point coordinates (r_i, z_i), $i = 1, \ldots, N$, where N is the number of mesh points, and are solved simultaneously with the governing physical equations for the velocity and pressure unknowns.

The mesh coordinate unknowns (r_i, z_i), like the velocity and pressure unknowns, are expanded using a set of finite element basis functions ϕ^i. For the sake of computational efficiency, the coordinates r and z are mapped onto the unit square in the computational domain with coordinates $\{(\xi, \eta) : 0 \leqslant \xi, \eta \leqslant 1\}$ using subparametric mapping, as described by Christodoulou & Scriven (1992) (see, also, Bathe 1982). Specifically, r and z are everywhere expanded using bilinear basis functions except along the free surface where 5-node basis functions with an extra node along the boundary are used to increase the accuracy of representing the curved shape of the filament.

A prerequisite for using the elliptic mesh generation technique is that the domain be divided into a number of quadrilateral subdomains, as illustrated in figure 2(*a*), with local coordinates (ξ_j, η_j), where $j = 1, 2, \ldots$, is the index of the subdomain. Since all integrations are performed upon mapping each element onto the computational

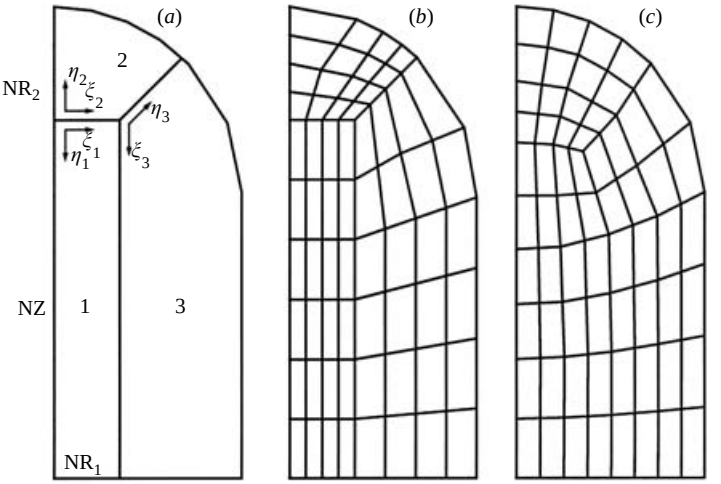

FIGURE 2. Three steps in generating a mesh for the initial filament shape: (*a*) the domain is subdivided into three quadrilateral regions or subdomains, (*b*) an algebraic mesh is constructed as an initial guess for the solution of the mesh equations, and (*c*) the mesh equations are solved to give the elliptic mesh solution.

domain with coordinates ξ and η, the mesh equations are written in what follows with respect to the (ξ, η) domain. The Galerkin weighted residuals of the pair of partial differential equations used to determine the unknown mesh coordinates (r_i, z_i) are (Christodoulou & Scriven 1992; Notz *et al.* 2001)

$$R^i_\xi = \int_A \left[\sqrt{\frac{r_\xi^2 + z_\xi^2}{r_\eta^2 + z_\eta^2}} + \epsilon_s \right] \nabla\xi \cdot \nabla\phi^i |J| \, \mathrm{d}\xi \, \mathrm{d}\eta - \epsilon_\xi \int_A f(\xi) \ln\left(r_\xi^2 + z_\xi^2\right) \phi^i_\xi \, \mathrm{d}\xi \, \mathrm{d}\eta$$

$$- M_\xi \int_{\partial A} f(\xi) \ln\left(r_\xi^2 + z_\xi^2\right) \phi^i_\xi \, \mathrm{d}\xi = 0, \quad i = 1, \ldots, N, \quad (3.1a)$$

$$R^i_\eta = \int_A \left[\sqrt{\frac{r_\eta^2 + z_\eta^2}{r_\xi^2 + z_\xi^2}} + \epsilon_s \right] \nabla\eta \cdot \nabla\phi^i |J| \, \mathrm{d}\xi \, \mathrm{d}\eta - \epsilon_\eta \int_A g(\eta) \ln\left(r_\eta^2 + z_\eta^2\right) \phi^i_\eta \, \mathrm{d}\xi \, \mathrm{d}\eta$$

$$- M_\eta \int_{\partial A} g(\eta) \ln\left(r_\eta^2 + z_\eta^2\right) \phi^i_\eta \, \mathrm{d}\eta = 0, \quad i = 1, \ldots, N. \quad (3.1b)$$

In (3.1), J is the determinant of the Jacobian of the transformation from the physical domain to the computational domain and ∂A is the boundary of the domain A. Simply put, (3.1*a*) and (3.1*b*) determine a set of curves of constant ξ and constant η that intersect at the mesh points. In (3.1), the parameter ϵ_s controls the smoothness of the mesh, i.e. of the curves of constant ξ and constant η, and is typically assigned a value that is $O(0.1)$. The parameters ϵ_ξ and ϵ_η control the concentration of the interior nodes and their values are typically $O(0.01)$–$O(1)$. The remaining parameters, M_ξ and M_η, are used to control the concentration of mesh points on the boundaries of the subdomains. Choosing M_ξ or M_η to be small, or zero, results in mesh coordinate curves that are nearly orthogonal to a boundary. By contrast, large values of M_ξ or M_η, i.e. of $O(10^3)$ or larger, cause the mesh to be distributed along a boundary according to the functions $f(\xi)$ and $g(\eta)$. The functions $f(\xi)$ and $g(\eta)$ are designed to

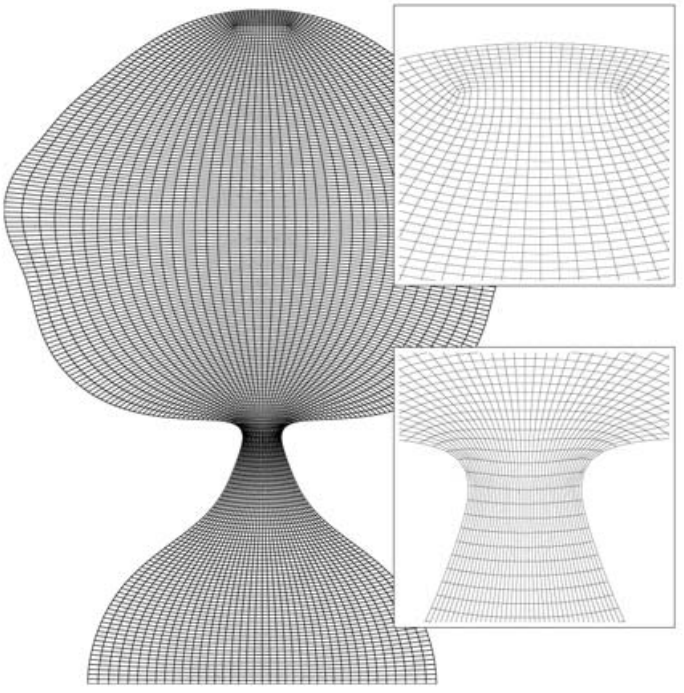

FIGURE 3. An example mesh when $Oh = 10^{-2}$ and $L_o = 15$ at $t = 10.990$. The top inset shows a closeup of the filament tip where the vertices of the three subdomains meet and the bottom inset shows a closeup of the neck region.

cause the mesh to concentrate (dilute) in the ξ- or η-directions where $f(\xi)$ or $g(\eta)$ are small (large). While these functions are beneficial for concentrating the mesh where desired, a poor choice of either $f(\xi)$ or $g(\eta)$ may lead to acute angles where the mesh coordinate curves intersect each other and the boundaries. Setting M_ξ or M_η to zero, however, can result in an undesirable mesh concentration along a boundary. Hence, the optimal choice for the mesh parameters and the functions $f(\xi)$ and $g(\eta)$ must be determined through experimentation.

In this paper, the mesh is concentrated axially where the filament necks and it is distributed nearly uniformly in the radial direction.

Once the domain has been subdivided into quadrilateral subdomains, as shown in figure 2(*a*), an algebraic mesh as shown in figure 2(*b*) is generated as an initial guess for the solution of the mesh equations. In order to solve the mesh equations over the entire domain, the subdomains are patched together through the boundary conditions on (3.1) (see Christodoulou & Scriven 1992; Notz *et al.* 2001). Along the external boundaries of the domain, physical conditions replace one of the mesh equations in order to determine the location of that boundary in physical space. The condition $r = 0$ is used in place of (3.1*a*) in subdomains 1 and 2 along the symmetry axis. The condition $z = 0$ is used in place of (3.1*b*) in subdomain 1 and (3.1*a*) in subdomain 3 along the mid-plane of symmetry. The kinematic boundary condition (2.3*b*) is used in lieu of (3.1*b*) in subdomains 2 and 3 along the free surface except when determining the initial mesh. At time $t = 0$, the analytic description of the initial filament shape is used for this purpose. The mesh equations are then solved to determine the locations of the mesh points, as shown in figure 2(*c*). An example mesh when $Oh = 10^{-2}$ and $L_o = 15$ at time $t = 10.990$ is shown in figure 3 (cf. figure 10 below).

As shown in figure 2, the number of elements deployed in meshes used in this work can be characterized by three independent parameters. Here NZ denotes the number of elements used in the η_1- and ξ_3-directions, NR_1 denotes the number of elements used in the ξ_1- and ξ_2-directions, and NR_2 denotes the number of elements used in the η_2- and η_3-directions. Moreover, $NR_1 \approx NR_2$ and their sum is defined as $NR = NR_1 + NR_2$. While $NZ \gg NR$, determination of appropriate values of these parameters requires systematic mesh refinement studies. This is a point that is returned to in § 3.3.

3.2. *Time integration and solution method*

Once the problem is discretized spatially with G/FEM, the result is a coupled system of nonlinear time-dependent differential-algebraic equations. This system of equations is integrated in time using an adaptive predictor–corrector method. The time derivatives at each step are calculated by either a first-order backward difference or a second-order trapezoid rule. Initially, eight backward difference steps are taken with a fixed step size to provide the necessary smoothing of the unphysical transients created by the inconsistent initial conditions (Luskin & Rannacher 1982; Brenan, Campbell & Petzold 1996). Thereafter, the trapezoid rule is used with time step size chosen to control time integration error (Gresho *et al.* 1980). Specifically, the step size is chosen by requiring the norm of the time truncation error at the next time step to be equal to a prescribed tolerance, typically 10^{-3}. A first-order forward difference predictor is used with the backward difference corrector and a second-order Adams–Bashforth predictor is used with the trapezoid rule corrector.

A system of nonlinear algebraic equations results after the spatial and time derivatives are discretized as just described. This system is solved using a fully coupled Newton's method with an analytically computed Jacobian. The system of algebraic equations resulting at each Newton iteration is solved using the frontal solver of Hood (1976) as modified and improved upon by Silliman (1979), Walters (1980), Coyle (1984), and Kheshgi & Scriven (1983). Newton iterations are continued until the L_2 norm of both the vector of residuals and the vector of updates falls below 10^{-6}. The correctness of the Jacobian is demonstrated by the quadratic convergence of Newton's method.

The algorithm is programmed in Fortran and is executed in serial on an IBM SP supercomputer consisting of WinterHawk-II 375 MHz Power3-II and WinterHawk 200 Mhz Power3 nodes. Convergence of the solution at each time step typically requires three to four Newton iterations.

3.3. *Accuracy checks and algorithm verification*

In order to determine an optimal mesh for a given L_o and Oh, the parameters NR and NZ must be independently varied until the computed solutions are insensitive to further systematic increases in the number of elements or mesh points used in the calculations. Table 1 summarizes the dimensions of the various meshes tested as well as the resulting number of degrees of freedom, or unknowns, and the average CPU time required per Newton iteration. Table 2 summarizes the results of the mesh sensitivity study for $L_o = 15$ when $Oh = 10^{-2}$ and $Oh = 10^{-3}$. The measures of the solution used are the dimensionless half-length of the drop at breakup L_b and the time to breakup t_b. Here breakup is said to have occurred when the minimum radius h_{min} of the filament falls below 2×10^{-3}. Table 2 makes clear that the computed solutions are virtually invariant for meshes II, III, V and VI. For both $Oh = 10^{-2}$ and $Oh = 10^{-3}$ the length at breakup and time to breakup differ by 1% or less between Mesh II and Meshes III, V, and VI. Therefore, Mesh II is used in analysing the

Mesh	NZ	NR	NEL	NDOF	CPU
I	100	10	1025	12260	1.9
II	200	10	2025	24160	3.7
III	300	10	3025	36060	5.5
IV	100	15	1556	18142	3.9
V	200	15	3056	35542	7.7
VI	300	15	4556	52942	11.5

TABLE 1. Characteristics of and execution times for the trial meshes used. Here, NEL is the total number of elements, NDOF is the number of degrees of freedom, and CPU refers to the average number of CPU seconds per Newton iteration.

	$Oh = 10^{-2}$		$Oh = 10^{-3}$	
Mesh	t_b	L_b	t_b	L_b
I	11.095	5.921	4.736	11.468
II	11.093	5.917	4.786	11.433
III	11.093	5.916	4.791	11.430
IV	11.096	5.920	4.736	11.468
V	11.092	5.917	4.787	11.433
VI	11.093	5.916	4.787	11.432

TABLE 2. Sensitivity of calculated solutions to mesh refinement for $L_o = 15$.

dynamics of the contracting filaments in the remainder of this paper unless otherwise indicated. One exception to the use of Mesh II is for filaments with initial lengths L_o exceeding 15 where a larger number of axial elements NZ must be used to attain the same level of accuracy as that shown in table 2.

The accuracy of the algorithm has been verified in three ways. First, the present algorithm is used to predict the oscillations of a viscous drop that is released from an initial static deformation. Predictions made with the new algorithm are compared with those of Basaran (1992) for the situation in which the initial drop shapes are prescribed in terms of spherical harmonics. In contrast to the present work, Basaran uses a spherical coordinate system with radial coordinate ϖ and polar-angle φ. Then, the initial deformed shape of the drop is $\varpi = f(\varphi)$, where the shape function $f(\varphi)$ is given by†

$$f(\varphi) = \gamma_n^{1/3}[1 + f_n P_n(\cos\varphi)], \qquad n = 2, 3, 4, \ldots . \tag{3.2}$$

Here γ_n is a constant scaling factor whose values are given by Basaran (1992), $P_n(\cdot)$ is the nth Legendre polynomial and f_n is a constant such that $f_n \ll 1$ for linearized oscillations and $f_n = O(1)$ for large-amplitude oscillations. The shape function in cylindrical coordinates is then $(r, z) = (\sin\varphi, \cos\varphi) f(\varphi)$ and $\varphi = \tan^{-1}(r/z)$.

Predictions made with the two algorithms have been compared for the cases where $n = 2$ with $f_2 = 0.9$ and $n = 4$ with $f_4 = 0.5$. Since Basaran (1992) uses a different mesh configuration than the one used in this work, his meshes cannot be exactly duplicated here; however, simulations have been performed with the new algorithm using a mesh resolution that is comparable to his. Drop shapes have been compared at various

† The exponent of 1/3 on γ_n in equation (3.2) is missing in the paper of Basaran (1992).

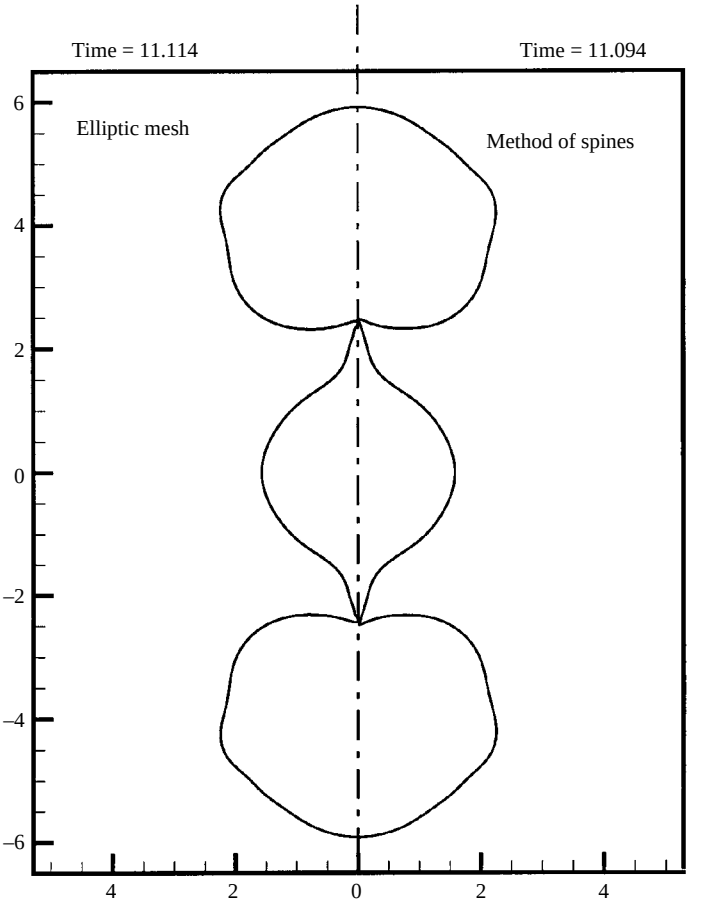

FIGURE 4. Comparison of the shapes at breakup when $Oh = 10^{-2}$ and $L_o = 15$ predicted by the G/FEM algorithm of this paper which is based on elliptic mesh generation (left) and the G/FEM algorithm of Wilkes *et al.* (1999) (see also Wilkes 1999) which is based on the method of spines (right).

instants in time by measuring drop shape functions at $r = 0$ (or $\varphi = 0$) and at $z = 0$ (or $\varphi = \pi/2$). At both locations, the difference in the value of the shape function has been found to be less than 1%.

Second, predictions made with the present algorithm have been compared to those made with the G/FEM algorithm of Wilkes *et al.* (1999) in analysing the dynamics of contracting filaments. The algorithm of Wilkes *et al.* (1999) uses the method of spines and has been well-tested against experimental measurements. Figure 4 shows a comparison of the predicted shapes at the incipience of breakup computed with the present algorithm (left) and the algorithm of Wilkes *et al.* (right). The excellent agreement between these predictions is further testimony to the accuracy of the present algorithm. The algorithm used here and that used by Wilkes *et al.* (1999) are identical in all respects with the exception of the method of domain discretization and mesh generation that they employ. First, the elliptic mesh generation method used in this paper, in contrast to the algorithm of Wilkes *et al.* (1999), does not require that the user have a qualitative *a priori* knowledge of the dynamics that will occur. Second, the new algorithm can go all the way from the onset of the motion to breakup

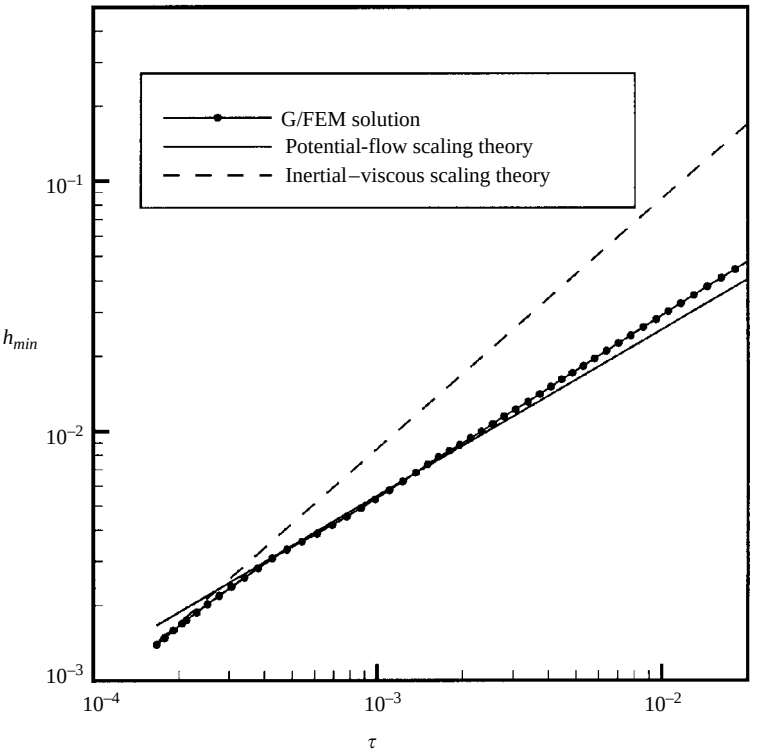

FIGURE 5. Computed variation of h_{min} with τ when $Oh = 10^{-2}$ and $L_o = 20$. Also shown are the potential flow scaling law, $h_{min} \sim \tau^{2/3}$, and the inertial–viscous scaling law, $h_{min} \sim \tau$.

without requiring any remeshing in all of the cases to be reported in this paper. By contrast, the algorithm of Wilkes *et al.* (1999) would require remeshing, albeit only a couple of times, to carry out the same computations. Third, the new algorithm is both more flexible and easier to program than that of Wilkes *et al.* (1999). Given that the two algorithms have virtually the same accuracy, the new algorithm is superior to the one used by Wilkes *et al.* (1999).

The third and final verification of the accuracy of the new algorithm is done by examining details of the local dynamics near the point of pinch-off. A number of authors have carried out local analyses of the Navier–Stokes, Stokes and Laplace equations for pinching threads (Keller & Miksis 1983; Eggers 1993; Papageorgiou 1995*a*,*b*; Day *et al.* 1998; Lister & Stone 1998; Papageorgiou & Orellana 1998; Eggers 2000). While algorithms based on the BEM, which are restricted to either Stokes flows or inviscid irrotational flows have been shown to be capable of describing accurately the pinch-off dynamics (Chen & Steen 1997; Day *et al.* 1998; Lister & Stone 1998), the only algorithms for solving the full Navier–Stokes equations which have demonstrated to have this level of accuracy are those used by Basaran and coworkers (Notz *et al.* 2001; Chen *et al.* 2002). Making computational predictions of the local dynamics that are mesh independent requires the use of finer discretizations than those listed in tables 1 and 2 (cf. Chen *et al.* 2002). Obtaining such solutions has required the use of a mesh with $NR_1 = NR_2 = 4$ and $NZ = 2000$. With these values of the mesh parameters, the finite element discretization involves 16 016 elements, 68 081 nodes, and 194 245 degrees of freedom. Figure 5 shows the variation of the minimum radius

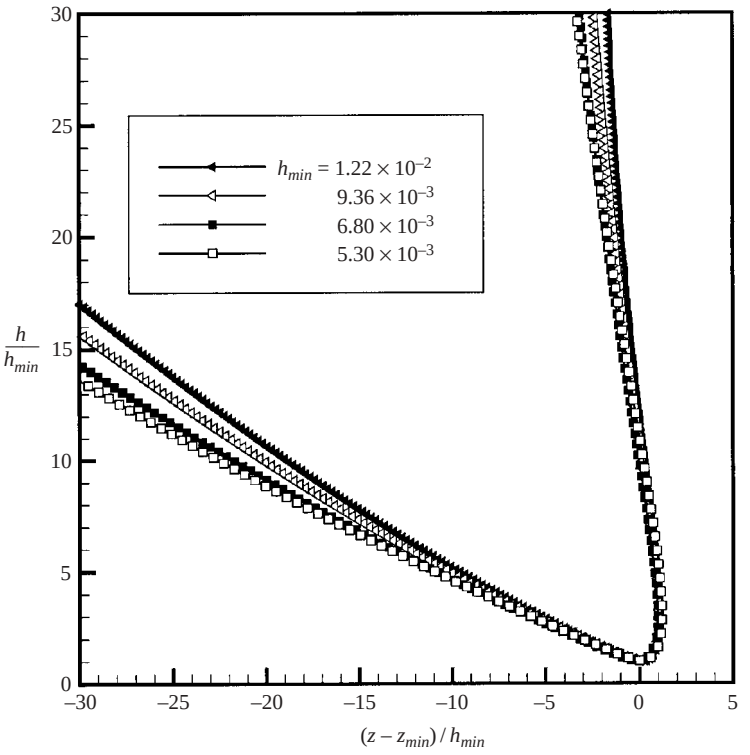

FIGURE 6. Variation of computed scaled drop profiles h/h_{min} with scaled axial coordinate $(z - z_{min})/h_{min}$ when $Oh = 10^{-2}$ and $L_o = 20$ (cf. figure 5) showing that the scaled shapes tend to the potential-flow similarity solution. With the exception of the scaled profile corresponding to the largest value of h_{min}, the value of h_{min} for each profile shown equals approximately 0.75 times the value of h_{min} for the profile that has the closest larger value of h_{min} to it.

h_{min} with time to breakup τ for the case when $Oh = 10^{-2}$ and $L_o = 20$. The calculations show that initially $h_{min} \sim \tau^{2/3}$, in accordance with the potential-flow scaling theory (Keller & Miksis 1983; Day *et al.* 1998). However, viscous effects eventually become important as the minimum radius continues to decrease and becomes order Oh^2, as shown by Eggers (1993). Indeed, the results depicted in figure 5 show the transition that takes place from the potential-flow to the inertial–viscous scaling regime, where $h_{min} \sim \tau$. The effect of the ambient gas on the dynamics may be neglected until $h_{min} \sim mOh^2$, where m is the ratio of the viscosity of the ambient fluid to that of the drop (Lister & Stone 1998).

Because of the orders of magnitude disparity between local length and time scales in the vicinity of pinch-off and corresponding global scales, interface shapes near h_{min} must be self-similar. To demonstrate the collapse of the computed interface shapes onto a similarity profile, figure 6 shows the variation of the interface thickness h scaled by the minimum radius h_{min}, h/h_{min}, with the scaled axial coordinate $(z - z_{min})/h_{min}$, where z_{min} is the axial coordinate at which $h = h_{min}$, for several values of τ when the dynamics falls in the potential flow regime. As time t increases, or time to breakup τ decreases, the scaled profiles h/h_{min} move away from the potential-flow similarity solution shown in figure 5 as viscous effects become locally important (not shown). Appropriately scaled computed interface profiles would eventually approach the inertial–viscous similarity solution once h_{min} falls below 10^{-4} (Eggers 1993; Chen

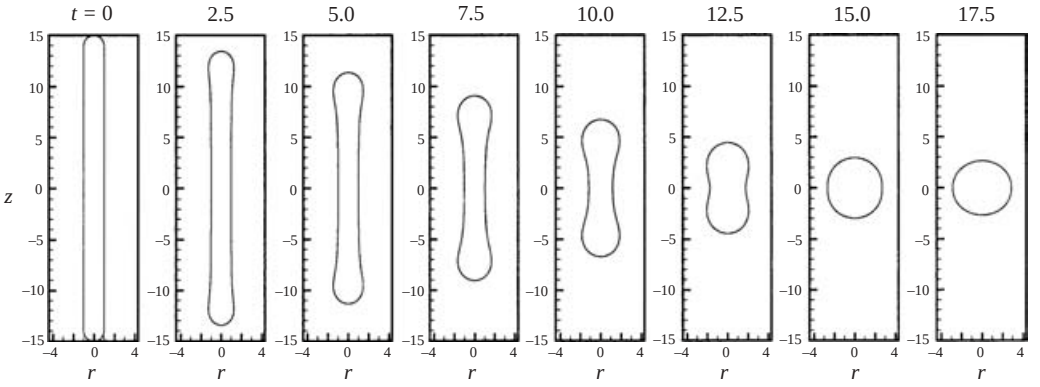

FIGURE 7. Time evolution of the shape of a contracting filament when $L_o = 15$ and $Oh = 1$.

et al. 2002). However, computation times become inordinately long when h_{min} falls below 10^{-3} and therefore it becomes prohibitive to demonstrate the approach to the inertial–viscous similarity profile for this value of Oh. Since the value of h_{min} for transition from the potential-flow to the inertial–viscous regime scales as Oh^2, the smaller (larger) the value of Oh the smaller (larger) is the value of h_{min} to which the calculations must be continued to observe the transition from one scaling regime to another. Unfortunately, if Oh is made larger than 10^{-2}, it is shown in the next section that a point is reached beyond which a contracting filament no longer breaks and hence it becomes impossible to observe the transition from the potential-flow to the inertial–viscous scaling regime. However, when a liquid drips from a capillary, the interface pinches off regardless of the value of Oh. Hence, the present algorithm has been generalized to also analyse drop formation from a capillary. First, it has been shown by repeating one of the calculations reported by Chen *et al.* (2002) for the situation in which $Oh = 1.63 \times 10^{-1}$ that both the potential-flow and inertial–viscous similarity solutions can be predicted by the new algorithm. Second, as a further test of the new algorithm, it has been demonstrated that computational results predicted with the algorithm used in this paper are within 0.1% of those reported by Chen *et al.* (2002).

4. Results and discussion

4.1. *Time evolution of shapes and breakup of contracting filaments*

In order to highlight the range of dynamics observed for contracting filaments, figures 7–10 show the evolution in time of the shapes of four filaments which all have an initial aspect ratio of $L_o = 15$ but are distinguished from each other by values of Oh that vary by three orders of magnitude between 10^{-3} and 1. After examining the dynamics for this set of parameters, the results for the whole parameter space will be presented.

For the situation in which $Oh = 1$, shown in figure 7, the filament evolves through a series of dog-bone shapes as it contracts and simply tends to a sphere at large times. Throughout the entire motion, the interface location remains a single-valued function of the axial coordinate z. When $Oh = 0.1$, shown in figure 8, the filament forms bulbous ends soon after it starts to contract. Although two distinct minima in the filament radius are apparent in this case, in contrast to the case when $Oh = 1$, the interface does not continue to constrict indefinitely. Thus, the filament fails to

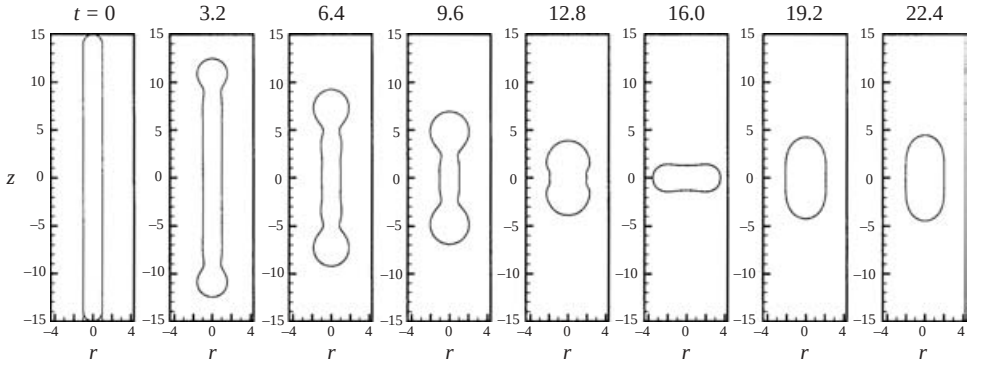

FIGURE 8. Time evolution of the shape of a contracting filament when $L_o = 15$ and $Oh = 0.1$.

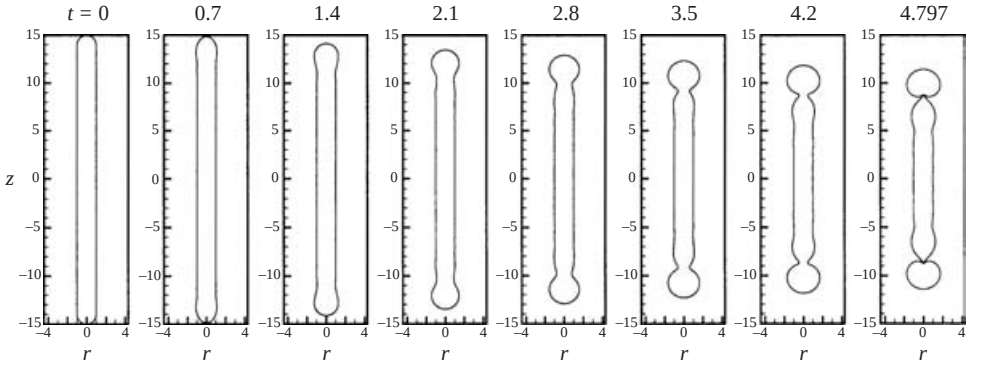

FIGURE 9. Time evolution of the shape of a contracting filament when $L_o = 15$ and $Oh = 10^{-3}$.

pinch-off the bulbous ends that form on it at early times. Instead, the filament simply thickens and its bulbous ends become larger. Hence, the filament undergoes a series of oscillations with ever diminishing amplitude, roughly one period of which is shown in figure 8. This filament too tends to a sphere at large times (not shown).

For very low values of Oh, such as $Oh = 10^{-3}$, shown in figure 9, the dynamics of the filament closely resemble those of a filament of an inviscid fluid undergoing irrotational flow (Schulkes 1996). Soon after this thread starts to contract, it forms bulbous ends similar to the case when $Oh = 0.1$ (cf. figure 8). However, capillary force dominates viscous force in this case and causes the bulbous ends to pinch-off from the filament. It is also noteworthy that the interface overturns on itself prior to breakup, as can be seen from the panel corresponding to $t = 4.797$ in figure 9.

The dynamics for the case when $Oh = 10^{-2}$, shown in figure 10, differ markedly from those at both large values of Oh (e.g. figures 7 and 8) and small values of Oh (e.g. figure 9). Initially, bulbous ends form on the contracting filament and it looks as if they will eventually pinch off, as shown by the two panels at $t = 3.22$ and 4.83 in figure 10. However, capillary forces are not large enough to overcome viscous forces and the emptying of the thinning necks is inhibited and pinch-off of the two bulbous ends via the endpinching mechanism is precluded in this case. Instead, the capillary waves on the surface of the filament evolve on a time scale comparable to the time required for the filament to contract to an aspect ratio of $O(1)$ and thereby lead to a peculiar shape at breakup.

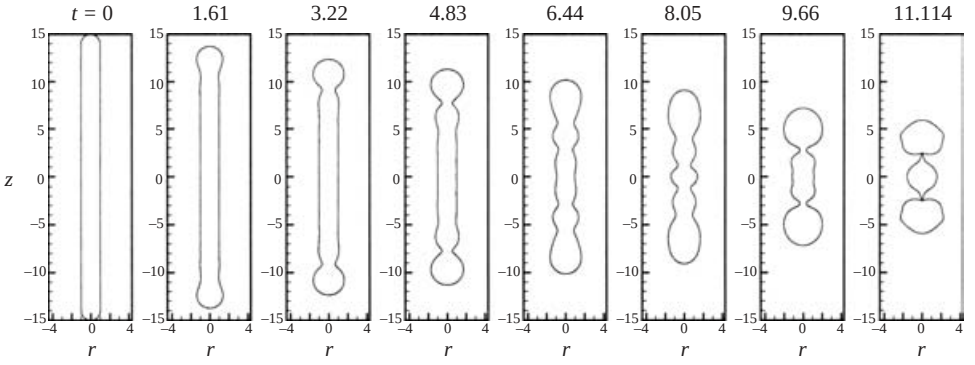

FIGURE 10. Time evolution of the shape of a contracting filament when $L_o = 15$ and $Oh = 10^{-2}$.

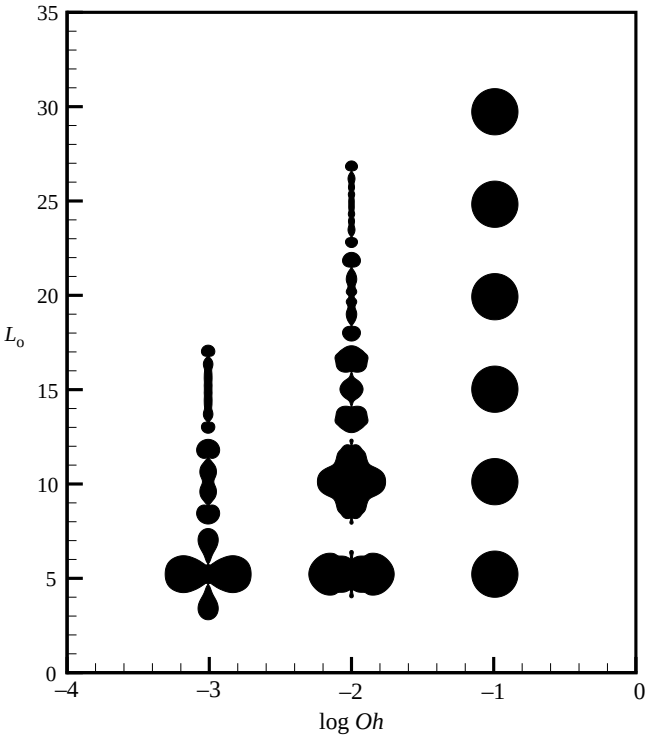

FIGURE 11. Final shapes of contracting filaments as a function of L_o and Oh. Shapes shown are not drawn to scale.

Figure 11 shows the final shapes of filaments of various values of Oh that are released from initial deformations characterized by the value of the initial aspect ratio L_o. For sufficiently large values of Oh, i.e. $Oh = O(0.1)$ or larger, the filaments do not break regardless of the value of the initial aspect ratio L_o. Such filaments simply relax to a sphere after undergoing a series of oscillations. For sufficiently small values of Oh, i.e. $Oh = O(0.01)$ or smaller, contracting filaments suffer three fates that depend on their initial deformations. Figure 11 makes plain that if L_o is sufficiently large, the filaments undergo an endpinching mode of breakup where daughter drops

Oh	10^{-3}	5×10^{-3}	10^{-2}	2.5×10^{-2}	5×10^{-2}
$L_{o,c}$	5.5 ± 0.5	8.75 ± 3.75	12.5 ± 2.5	17.5 ± 2.5	27.5 ± 2.5

TABLE 3. Variation with Ohnesorge number of the critical initial aspect ratio $L_{o,c}$ below which a filament does not break.

break off from the two ends of contracting filaments. At intermediate values of L_o, the dynamics are quite complicated and result in a variety of shapes at breakup, as shown in figure 11. When L_o is sufficiently small, the filaments do not break but tend to a sphere after undergoing a series of oscillations (not shown but see e.g. Basaran 1992).

Thus, there exists both (i) a critical Ohnesorge number Oh_c above which a contracting filament does not break no matter how large the initial aspect ratio and (ii) a critical initial aspect ratio $L_{o,c}$, at any value of Oh for which filament breakup occurs, below which a filament does not break. In his pioneering study, Schulkes (1996) surmized that $5\times10^{-3}\leqslant Oh_c\leqslant10^{-2}$ despite that he could not continue his calculations to breakup. With the present algorithm, it has been found that endpinching occurs for Oh as large as 5×10^{-2} provided that the initial aspect ratio L_o is sufficiently large. Schulkes (1996) further estimated that in order to prevent the full contraction before breakup of a filament, an initial aspect ratio of $L_o\equiv L_{o,c}\geqslant8$ is required. Table 3 shows that the critical value of the initial aspect ratio for breakup $L_{o,c}$ strongly depends on the value of Oh: whereas any filament of initial aspect ratio $L_o\geqslant5.5\pm0.5$ will break when $Oh=10^{-3}$, $L_o\geqslant27.5\pm2.5$ for breakup to occur when $Oh=5\times10^{-2}$.

Calculations also show that for $Oh\leqslant10^{-2}$, a limiting value of the initial aspect ratio exists above which further increases in the value of L_o insignificantly affect the time to breakup t_b. For example, when $Oh=5\times10^{-3}$, whereas $t_b=7.4$ when $L_o=12.5$, $t_b=9.8$ when $L_o=15$ but $t_b=10.4$ when $L_o=17.5$ as well as when $L_o=30$.

In their recent study of filaments formed during the pinch-off of drops from a tube, Henderson *et al.* (2000) report an exact solution of the Navier–Stokes equations for a cylindrical filament undergoing uniform, axial extension or contraction with or without surface tension, with or without viscosity, and in the presence or absence of gravity. From their analytic solution, they obtain a simple expression that the filament thickness varies with time as $h(t)=K/\sqrt{T-t}$, where K and T are constants. Based on their experimental observations, these authors demonstrate that their solution holds well for the thinning neck of a drop in drop formation prior to pinch-off in situations where the thread thickness is nearly uniform in the axial direction. However, these authors have also noted that the analytical solution does not appear to hold for the contracting satellites that are formed once the thread separates from the primary drop and the liquid attached to the tube. The results presented here illustrate that even though the filament thickness is nearly uniform in the axial direction during the initial stages of contraction, the filament does not contract uniformly for all times and so the results presented here also do not agree well with the analytic solution of Henderson *et al.* (2000). This difference in behaviour can be understood by examining the forces driving the contraction of filaments.

At $t=0$, the value of twice the dimensionless mean curvature along the cylindrical body of the filament is $-2\mathscr{H}=1$ whereas that along the two hemispherical ends of the filament is $-2\mathscr{H}=2$. Thus, in accord with the normal stress boundary condition (2.3*a*) at the free surface, a pressure gradient exists initially near the two ends of

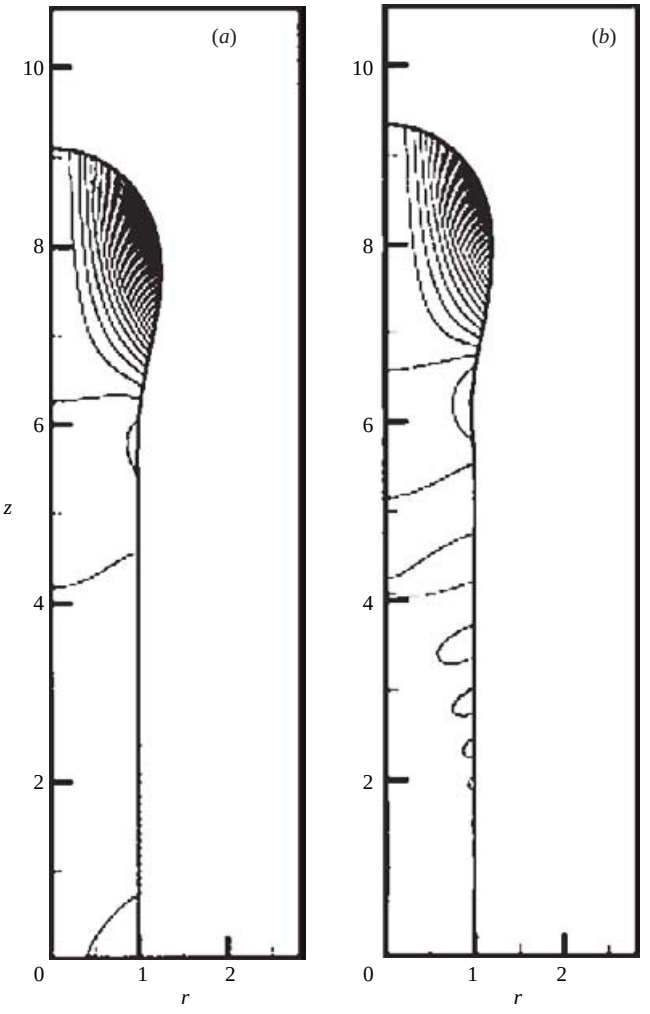

FIGURE 12. Streamlines in contracting filaments of $L_o = 10$: (*a*) $Oh = 0.1$ at $t = 1.639$ and (*b*) $Oh = 10^{-2}$ at $t = 1.318$. For the streamlines shown, values of the stream function range from -0.6 to 0.05 in increments of 0.025.

the filament. The pressure gradient drives fluid from the tips toward the centre of the filament. As the accelerating fluid from the tips collides with the quiescent fluid nearer the centre of the filament, the fluid is forced to flow radially outward causing the ends of the filament to bulb up. Eventually, an internal shear layer develops causing the fluid nearer the centre of the filament to also flow radially outward. This is demonstrated in figure 12 where the instantaneous streamlines are plotted in two filaments with the same initial aspect ratio of $L_o = 10$ but with different Ohnesorge numbers of $Oh = 0.1$ and 10^{-2}. Hence, the contraction of the filament initially occurs mainly at its ends while the fluid in the larger central region of the filament is essentially quiescent and does not participate in this motion. Thus, the central region in the filament initially maintains a thickness that is nearly uniform in both space and time. When the central region of the filament eventually begins to thicken, it does so, however, with a non-uniform thickness.

4.2. *Comparisons with predictions made with the slender-jet approximation*

Several researchers (Brenner *et al.* 1997; Ambravaneswaran *et al.* 2000, 2002) have recently demonstrated that predictions based on the slender-jet approximation (Bechtel, Cao & Forest 1992; Eggers 1993; Eggers & Dupont 1994; Papageorgiou 1995*b*) can be both efficient and accurate in predicting drop dynamics. However, assumptions inherent in the slender-jet approximation may preclude its use in some situations. Most obvious is the assumption that the interface location is a single-valued function of the axial coordinate, namely $r = h(z, t)$. However, it is unclear at the present time when the leading-order solution based on the slender-jet approximation may be sufficient to describe the dynamics of contracting filaments with reasonable accuracy. In this section, the formulation of the one-dimensional slender-jet equation is briefly summarized and comparisons between predictions based on the slender-jet approximation and those based on the full two-dimensional system of equations are made.

In the slender-jet approximation, the interface location is assumed to be given by a single-valued function $r = h(z, t)$, and the axial velocity and pressure are expanded in a Taylor series in the radial coordinate

$$v(r, z, t) = v_0(z, t) + v_2(z, t)r^2 + \cdots, \tag{4.1a}$$

$$p(r, z, t) = p_0(z, t) + p_2(z, t)r^2 + \cdots. \tag{4.1b}$$

In (4.1), $v_n(z, t)$ and $p_n(z, t)$, where $n = 0, 2, \ldots$, are the unknown functions that are to be determined. In order to satisfy continuity (2.1*b*), the radial velocity must have the form

$$u(r, z, t) = -\frac{r}{2}\frac{\partial v_0}{\partial z} + \cdots. \tag{4.2}$$

The expansions (4.1) and (4.2) are substituted into the momentum equations (2.1) and the boundary conditions (2.3) at the free surface are used to simplify the resulting system of equations. The leading-order asymptotic equations that result are (cf. Eggers 1993)

$$\frac{\partial v_0}{\partial t} = -v_0\frac{\partial v_0}{\partial z} - \frac{\partial 2\mathscr{H}}{\partial z} + 3Oh\frac{1}{h^2}\frac{\partial}{\partial z}\left(h^2\frac{\partial v_0}{\partial z}\right), \tag{4.3a}$$

$$\frac{\partial h}{\partial t} = -v_0\frac{\partial h}{\partial z} - \frac{1}{2}h\frac{\partial v_0}{\partial z}, \tag{4.3b}$$

$$2\mathscr{H} = \frac{1}{h[1 + (\partial h/\partial z)^2]^{1/2}} - \frac{\frac{\partial^2 h}{\partial z^2}}{[1 + (\partial h/\partial z)^2]^{3/2}}. \tag{4.3c}$$

Although it is not strictly correct to retain the expression for the full curvature in (4.3*c*), previous studies have shown that doing so greatly increases the accuracy of one-dimensional analyses (Eggers & Dupont 1994; Brenner *et al.* 1997; Ambravaneswaran *et al.* 2002).

Figure 13 compares predictions of contracting filaments made using the one-dimensional equations with ones made using the full two-dimensional equations for $L_o = 15$ when $Oh = 1, 10^{-2}$ and 10^{-3}. When $Oh = 1$, the filament does not break and so the predictions made with the two methods are compared at an intermediate time $t = 8$ (cf. figure 7). When $Oh = 10^{-3}$, the interface of the filament as predicted by the two-dimensional algorithm overturns shortly before breakup and so the one-dimensional predictions depart slightly from their two-dimensional counterparts near the points of pinch-off.

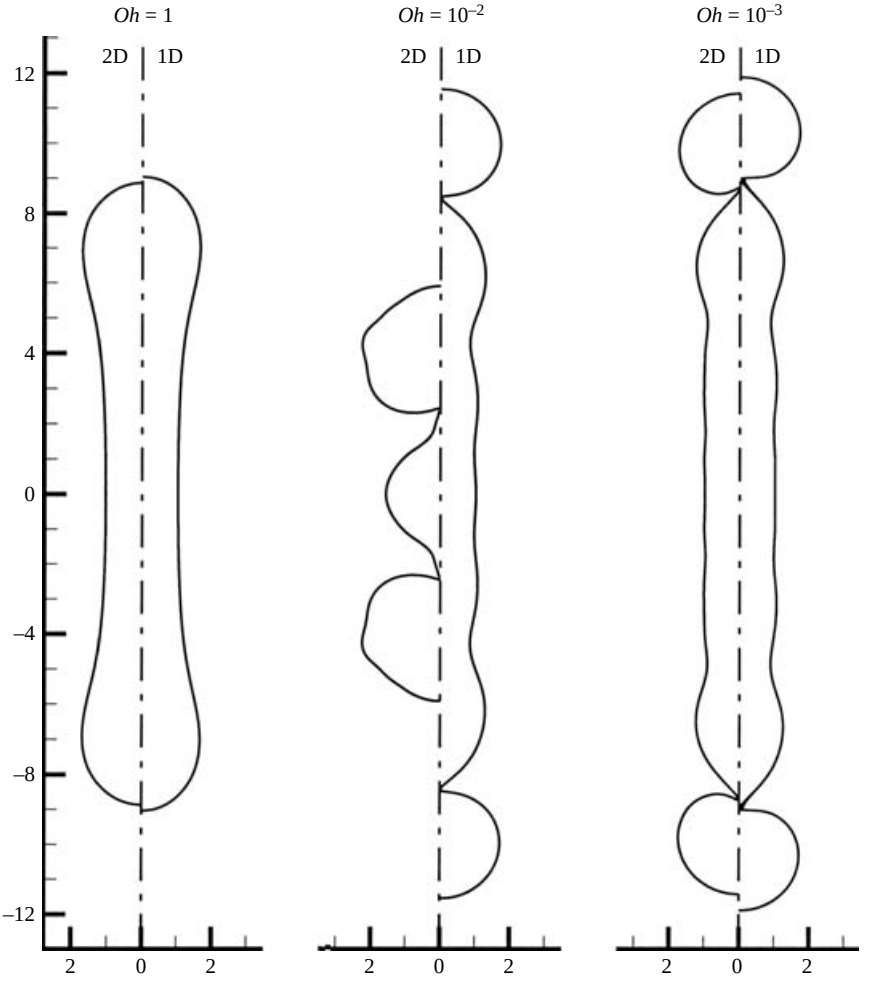

FIGURE 13. Comparison of filament shapes predicted by the two-dimensional G/FEM algorithm of this paper (2D) and those predicted by slender-jet analysis using the one-dimensional G/FEM algorithm of Ambravaneswaran (2000) (see also Ambravaneswaran *et al.* 2002) (1D). In all three cases, the filaments have the same initial aspect ratio of $L_o = 15$.

While figure 13 makes clear that the one-dimensional predictions agree quite well with their two-dimensional counterparts for large and small values of *Oh*, the one-dimensional predictions differ significantly from the two-dimensional predictions at intermediate values of *Oh*. Interestingly, the one-dimensional predictions begin to deviate from the two-dimensional predictions at the intermediate value of *Oh* long before the interface becomes a multivalued function of the axial coordinate. Clearly, the leading-order equations (4.3) do not accurately describe the dynamics in this region of the parameter space. One way to understand why the one-dimensional slender-jet approximation fails at intermediate values of *Oh* is to investigate the vorticity $\boldsymbol{w} = \nabla \times \boldsymbol{v}$ in the contracting filament.

4.3. *Vorticity dynamics*

The goal behind examining the vorticity dynamics is to investigate the competition between the generation of vorticity due to the motion of the curved free surface

and the dissipation of vorticity due to viscous effects in a contracting filament. The well-known vorticity equation is obtained by computing the curl of the momentum equation (2.1*a*) (Panton 1996):

$$\frac{\mathrm{D}\boldsymbol{w}}{\mathrm{D}t} = \boldsymbol{w}\cdot\nabla\boldsymbol{v} + Oh\nabla^2\boldsymbol{w}. \tag{4.4}$$

The first term on the right-hand side accounts for vorticity generation due to stretching of vortex lines and the second term there represents vorticity diffusion.

In addition to vorticity, it is also useful here to examine the enstrophy, $\omega = \frac{1}{2}\boldsymbol{w}\cdot\boldsymbol{w}$, which is one half the square of the magnitude of the vorticity. Contracting (4.4) with the vorticity leads to the enstrophy conservation equation. Using the vector identity $\frac{1}{2}\nabla^2 w^2 = \boldsymbol{w}\cdot\nabla^2\boldsymbol{w} + \nabla\boldsymbol{w}:\nabla\boldsymbol{w}$, the enstrophy equation becomes (Panton 1996)

$$\frac{\mathrm{D}\omega}{\mathrm{D}t} = \boldsymbol{w}\cdot\boldsymbol{D}\cdot\boldsymbol{w} + Oh\nabla^2\omega - Oh\Phi_w \tag{4.5}$$

where $\boldsymbol{D} = \frac{1}{2}[\nabla\boldsymbol{v} + (\nabla\boldsymbol{v})^T]$ is the rate of deformation tensor and $\Phi_w = \nabla\boldsymbol{w}:(\nabla\boldsymbol{w})^T \geqslant 0$ is the vorticity dissipation function. From equations (4.4) and (4.5), it is clear that both the diffusion and the dissipation of vorticity throughout the domain are proportional to Oh.

Integration of (4.4) over a volume of fluid $V(t)$ bounded by a free surface $S_f(t)$ leads to the macroscopic vorticity balance

$$\frac{\mathrm{D}}{\mathrm{D}t}\int_{V(t)} \boldsymbol{w}\,\mathrm{d}V = \int_{V(t)} \boldsymbol{w}\cdot\nabla\boldsymbol{v}\,\mathrm{d}V + 2Oh\int_{S_f(t)} \boldsymbol{e}_\theta\boldsymbol{n}\cdot\nabla\left(\frac{\partial v_n}{\partial s} + \kappa_s v_s\right)\mathrm{d}S. \tag{4.6}$$

In (4.6), V, S and s stand for volume, surface area and arc length, respectively, $\boldsymbol{e}_\theta$ is a unit vector in the azimuthal direction, v_n and v_s are the normal and tangential components of the fluid velocity along the free surface and κ_s is the principal curvature of the free surface in the plane of flow. What is new and important for the situation under study is the surface integral in (4.6). It represents the generation of vorticity at the free surface which is, first of all, proportional to Oh. The first term in the surface integral represents vorticity generation due to the shear flow that is directed perpendicular to the free surface. The second term in the surface integral represents the vorticity generation due to the normal gradient of the flow that is directed along the curved boundary of the filament–ambient fluid interface.

For small values of Oh, there is very little generation of vorticity at the free surface. Furthermore, any vorticity generated there takes a long time to diffuse into the interior of the domain. Thus, for small values of Oh the flow in the filament remains nearly irrotational for all times. For large values of Oh, the vorticity generated at the free surface rapidly diffuses throughout the domain where it dissipates quickly. Thus, for large values of Oh, the flow in the filament appears nearly irrotational. For intermediate values of Oh, however, vorticity generation is sufficiently large and the dissipation of vorticity is sufficiently small that the velocity field contains a significant rotational component. These points are illustrated in figure 14 where vorticity contours are plotted for three filaments of $L_o = 15$ when $Oh = 1, 10^{-2}$ and 10^{-3}. Because the majority of the vorticity is generated near the location where the filament's radius is smallest due to the high curvature and large velocity gradients there, only that portion of the filament is shown for clarity in figure 14.

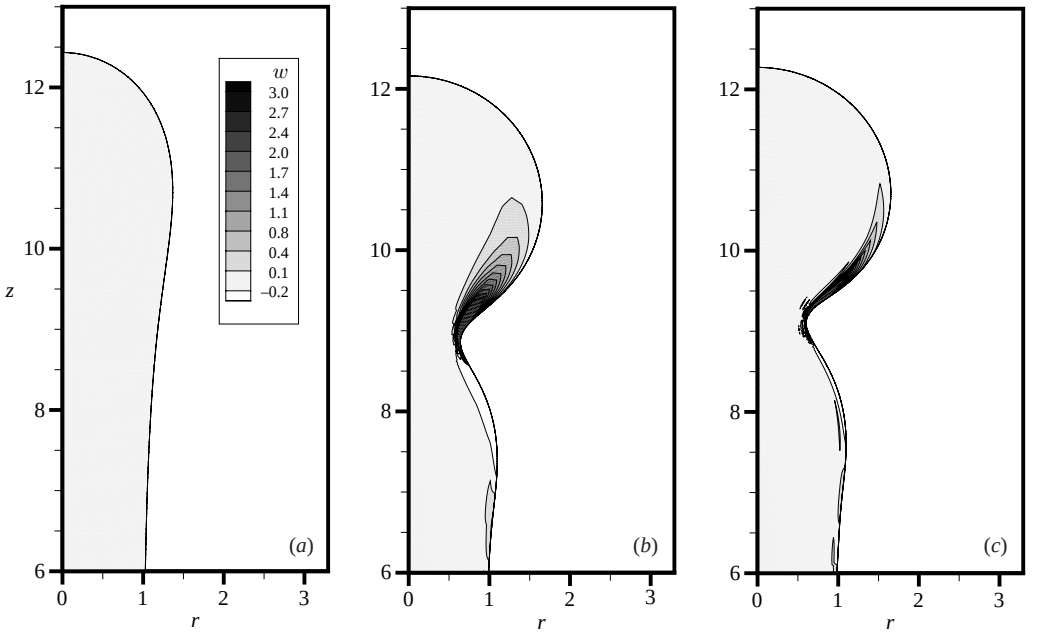

FIGURE 14. Vorticity fields in contracting filaments of $L_o = 15$: (*a*) $Oh = 1$ at $t = 4.283$, (*b*) $Oh = 10^{-2}$ at $t = 3.992$, and (*c*) $Oh = 10^{-3}$ at $t = 2.847$. Values of vorticity shown in (*a*) apply in all three situations.

For an axisymmetric flow, the vorticity is purely in the azimuthal direction and is given by $w_\theta = \partial u/\partial z - \partial v/\partial r$. This vorticity in the one-dimensional slender-jet approximation is given by

$$w_\theta = -\frac{r}{2}\frac{\partial^2 v_0}{\partial z^2} - 2r v_2 + \cdots. \tag{4.7}$$

Equation (4.7) makes plain that the vorticity is an $O(r)$ quantity in the slender-jet approximation. Thus, for the one-dimensional approximation to hold, the vorticity needs to be small throughout the domain. Therefore, the results depicted in figure 14 and equation (4.7) make clear why the one-dimensional approximation fares poorly at intermediate values of *Oh*.

4.4. *Velocity and pressure fields within contracting filaments*

Given the results of the previous two subsections and certain findings reported by Schulkes (1996), it is worthwhile to examine velocity and pressure fields within contracting filaments. Here these fields are examined when $Oh = 0.1$, 0.001, and 0.01 for filaments with initial aspect ratios $L_o = 15$. The situation for which $Oh = 1$ is not repeated here since Schulkes' (1996) algorithm was able to capture the entire dynamics as the initially highly elongated filament contracted to a sphere without breaking for this value of *Oh* (cf. figure 7). Schulkes (1996) showed that when $Oh = 1$, all the velocity vectors for $r > 0$ pointed in the same direction as the filament contracted to a sphere.

Figures 15–17 show at several instants in time the shapes of filaments and the variation with the axial coordinate of the axial velocities and pressures along the centrelines of the filaments, $v_a \equiv v(r = 0, z, t)$ and $p_a \equiv p(r = 0, z, t)$, respectively, for

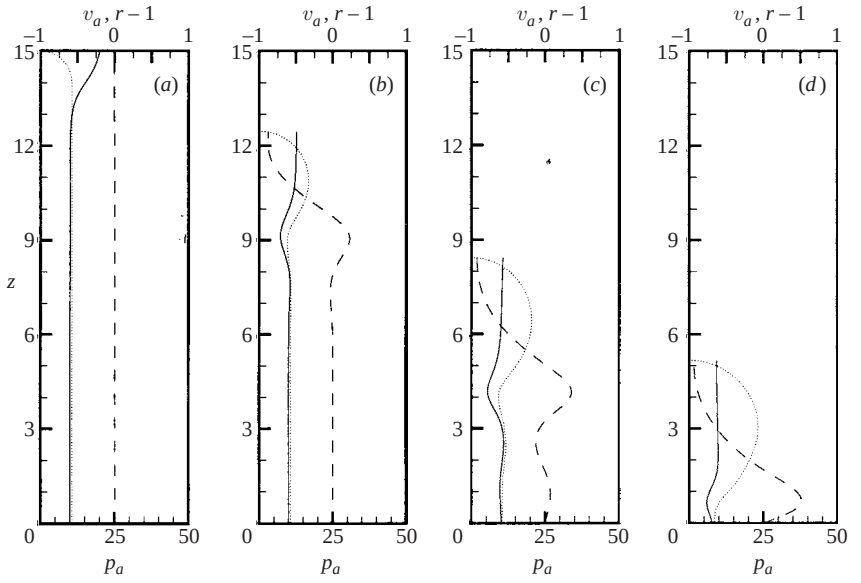

FIGURE 15. Evolution in time of the shape (dotted line) and the axial velocity v_a (dashed line) and the pressure p_a (solid line) along the centreline of a contracting filament when $Oh = 0.1$ and $L_o = 15$. The radial coordinates of the filament profile and the values of v_a are shown on the top axis and the values of p_a are shown on the bottom axis. Moreover, to make the figures clearer, values of $r - 1$ rather than r are plotted as a function of z in depicting the filament shapes. (*a*) $t = 4 \times 10^{-3}$, (*b*) $t = 3.457$, (*c*) $t = 8.086$, and (*d*) $t = 11.515$.

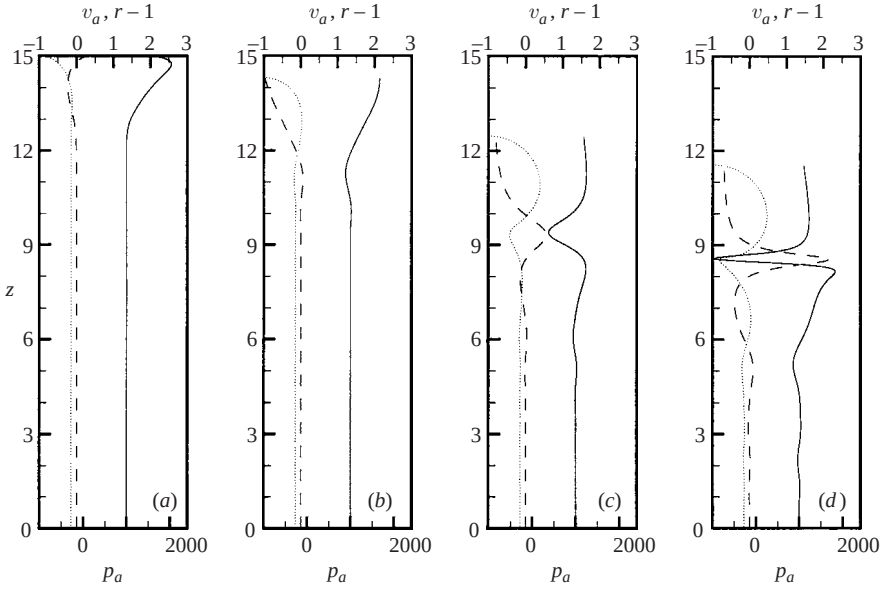

FIGURE 16. As figure 15 but $Oh = 0.001$ and (*a*) $t = 0.345$, (*b*) $t = 1.339$, (*c*) $t = 3.385$, and (*d*) $t = 4.603$.

these three values of Oh. A one-dimensional slender-jet algorithm would also provide information akin to that provided by figures 15–17 since at a given value of the axial coordinate, neither the axial velocity nor the pressure vary with the radial coordinate

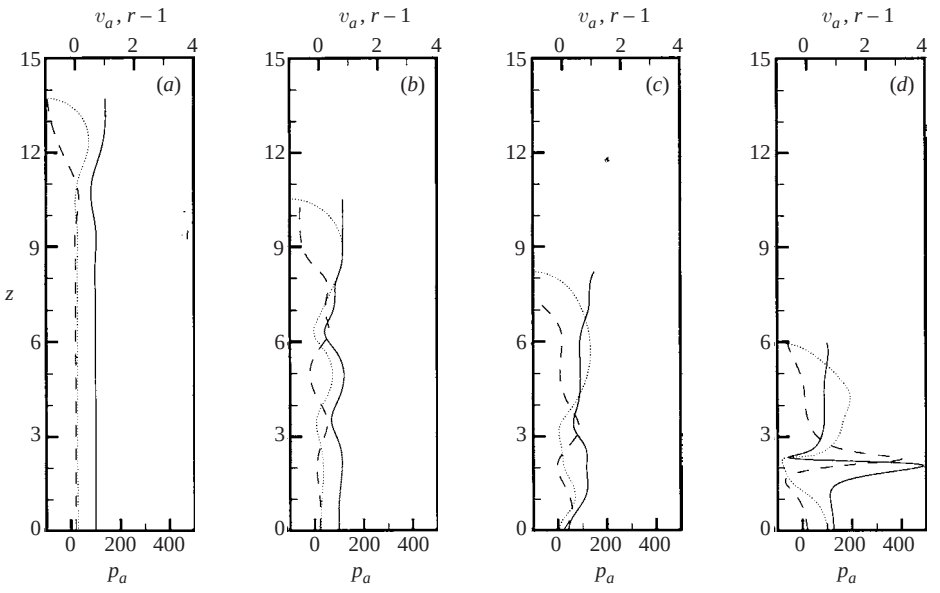

FIGURE 17. As figure 15 but when $Oh = 0.01$ and (*a*) $t = 1.952$, (*b*) $t = 6.107$, (*c*) $t = 8.910$, and (*d*) $t = 11.005$.

in the slender-jet approximation (cf. § 4.2). Figures 18–20 show at the same instants in time the velocity and pressure fields throughout these filaments. These figures show that in contrast to the situation when $Oh = 1$, the velocity fields exhibit several stagnation points along the axis of symmetry when $Oh \leqslant 0.01$, as has already been noted by Schulkes (1996). Moreover, several minima in pressure can be observed in each of these figures, each corresponding to a local minimum in filament radius. For $Oh = 0.1$, Schulkes was able to continue his calculations until the point in time when the recoiling filament's radius in the equatorial plane of symmetry $z = 0$ started to increase in time. For $Oh = 0.01$, Schulkes was not able to continue his calculations beyond the instant in time when the filament radius was still larger than 0.8 and he does not report results for $Oh = 0.001$.

While the situation in which $Oh = 0.01$ is qualitatively similar to those in which $Oh = 0.1$ and 0.001, two features distinguish the former situation from the latter two. When $Oh = 0.01$, a zone of recirculation forms inside the recoiling bulbous tip of the filament for values of the axial coordinate just exceeding that at which the filament radius is a minimum, as shown in figure 20. Such a recirculating flow, where the axial velocity takes on both positive and negative values at a given value of the axial coordiate, is a direct manifestation of the importance of vorticity in a recoiling filament at this value of Oh and cannot be predicted by the one-dimensional slender-jet approximation. The demonstration in the previous section of the presence of substantial amounts of vorticity within a filament and that in this section of the existence of a recirculating eddy within the same filament make plain why the one-dimensional slender-jet approximation fails to describe accurately the dynamics when $Oh = 0.01$. Figures 18–20 also show that except near locations where the filament is pinching, the computed contour lines of pressure are nearly horizontal and agree well

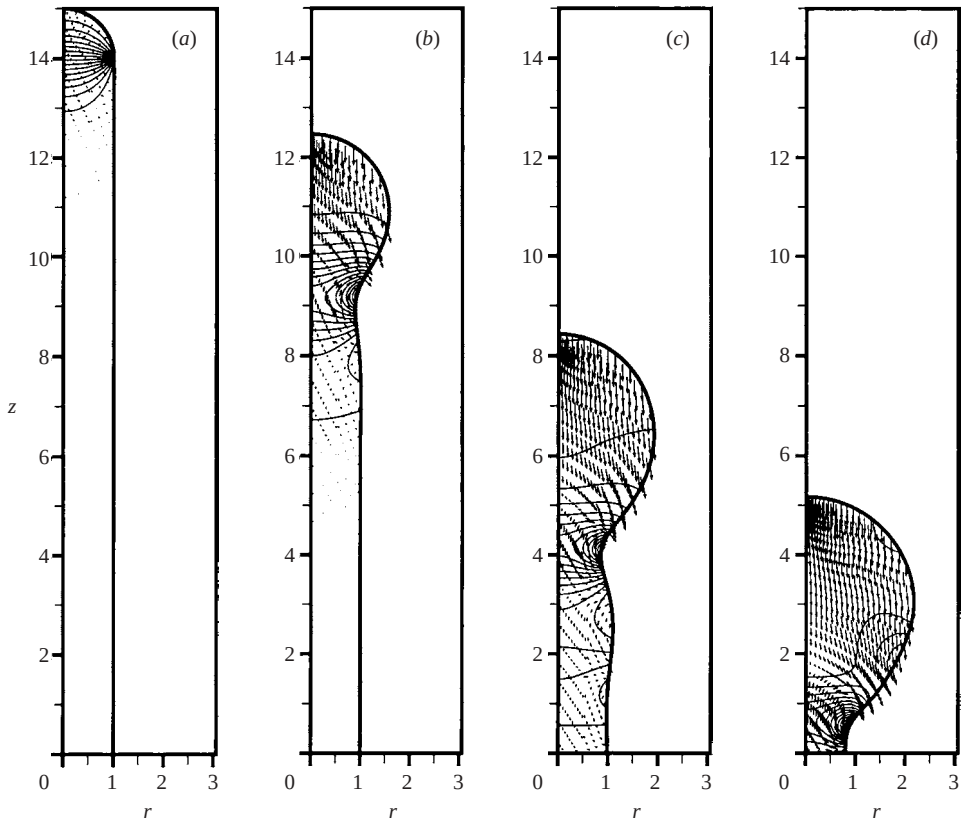

FIGURE 18. Evolution in time of the velocity and pressure fields within a contracting filament when $Oh = 0.1$ and $L_o = 15$. The arrows represent the fluid velocity at a given point in the filament and each velocity vector shown belongs to its base point. The curves shown are contour lines of pressure. (*a*) $t = 4 \times 10^{-3}$, (*b*) $t = 3.457$, (*c*) $t = 8.086$, and (*d*) $t = 11.515$.

with the built-in assumption of the one-dimensional slender-jet approximation that the pressure is independent of the radial coordinate when $Oh = 0.1$ and 0.001.

4.5. *Time evolution of the aspect ratio and tip velocity of contracting filaments*

Figure 21 shows the variation with time t of $1 - L/L_o$, where L is the instantaneous half-length of a contracting filament, for several Ohnesorge numbers. Whereas figure 21(*a*) depicts the time evolution of $1 - L/L_o$ over the entire range of times over which the dynamics take place, figure 21(*b*) highlights the dynamics during the early times of recoiling for the two high-viscosity filaments ($Oh = 1$ and 0.1) and until they break for the two low-viscosity filaments ($Oh = 0.01$ and 0.001). These figures show that since the inception of the motion, the motion of the tip of a filament with $Oh = 0.001$ virtually follows that of a filament with $Oh = 0.01$ until the filament with $Oh = 0.001$ breaks.

Figure 22 shows how the velocity of the tip of a filament $v_{tip} \equiv \mathrm{d}L/\mathrm{d}t = v(r = 0, z = L(t), t)$ varies with time t for the same four filaments of figure 21. Figure 22 makes plain that in each case, the filament tip initially accelerates upon the onset of the dynamics but then decelerates after the elapse of a certain amount of time

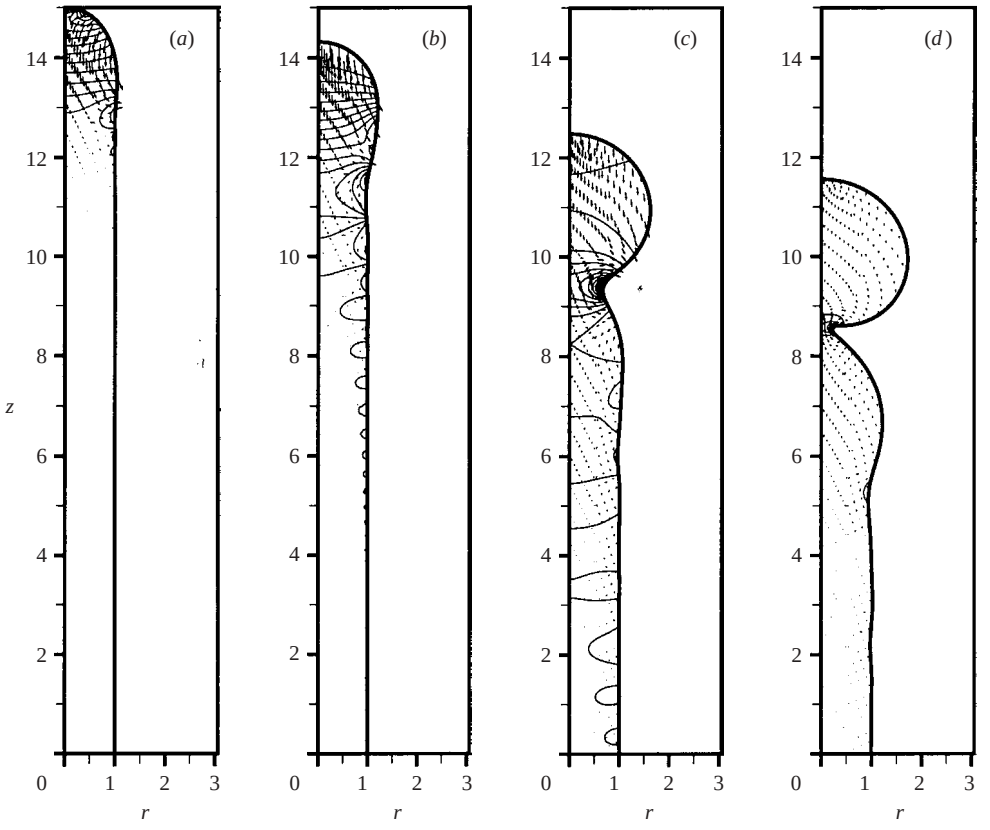

FIGURE 19. As figure 18 but when $Oh = 0.001$ and (*a*) $t = 0.345$, (*b*) $t = 1.339$, (*c*) $t = 3.385$, and (*d*) $t = 4.603$.

that increases with increasing Oh. The filament when $Oh = 0.001$ breaks after its tip starts to decelerate, as shown in figure 22. By contrast, the filament when $Oh = 0.01$ starts a second period of acceleration but ultimately breaks once its tip has slowed down to a speed approximately equal to the value it had when its tip had begun to accelerate again. Figures 21 and 22 further depict that the filaments when $Oh = 0.1$ and 1 undergo underdamped and overdamped oscillations, as already discussed in § 4.1.

It is also worthwhile to compare the computed predictions reported in figures 21 and 22 to the calculations reported by Schulkes (1996) and the works of Keller *et al.* (1995), Ting & Keller (1990) and Keller (1983), who showed that the tip of an inviscid filament of uniform radius can contract at a constant velocity. The preliminary results of Schulkes (1996) and the results of figures 21 and 22 clearly show that for low-Oh filaments, there does not exist a finite period of time during which the tip of a contracting filament moves at a constant velocity.

5. Conclusions

A powerful G/FEM algorithm has been developed which has made it possible to study the dynamics of contracting filaments all the way to breakup at finite Ohnesorge

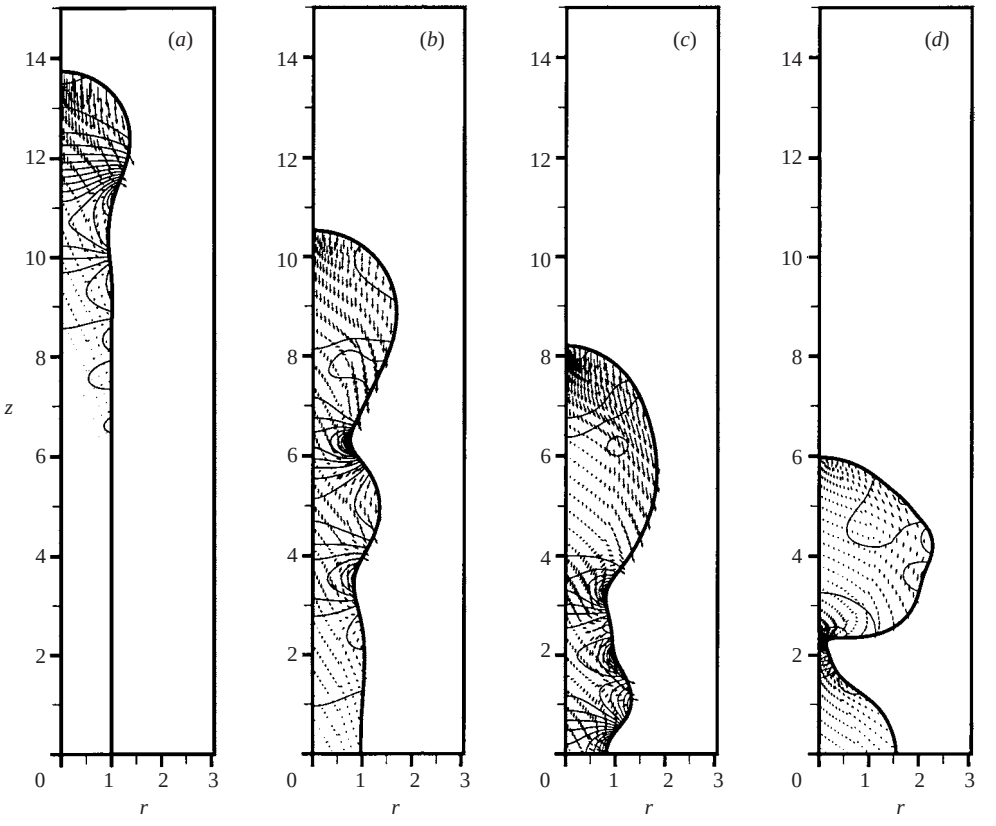

FIGURE 20. As figure 18 but when $Oh = 0.01$ and (*a*) $t = 1.952$, (*b*) $t = 6.107$, (*c*) $t = 8.910$, and (*d*) $t = 11.005$.

number Oh or Reynolds number $Re \equiv Oh^{-1}$ (cf. Schulkes 1996). It is shown that when $Oh \gtrsim O(0.1)$, the filaments ultimately contract to their equilibrium spherical shapes without breaking into multiple droplets regardless of their initial aspect ratio. When $Oh \lesssim O(0.1)$, filaments with sufficiently large initial aspect ratios pinch-off daughter drops from their ends through the so-called endpinching mechanism. For smaller values of the initial aspect ratio L_o, filaments undergo a series of complex oscillations which ultimately lead to breakup. For a yet smaller L_o, filaments evolve to their equilibrium spherical shapes after undergoing a sequence of complex oscillations.

The predictions of the dynamics of contracting filaments made with the G/FEM algorithm are compared to those made with a one-dimensional model based on the slender-jet approximation. The two predictions are in good agreement for both large and small Oh with the limitation that the one-dimensional models are inherently incapable of predicting dynamics which involve interface shapes that are multivalued functions of the axial coordinate or exhibit interface overturning. However, at intermediate values of Oh, significant disagreement exists between the two models. This discrepancy is explained by demonstrating that (*a*) the one-dimensional models are only accurate when the magnitude of the vorticity is small, i.e. $w_\theta = O(r)$, and (*b*) the vorticity of the fluid is maximized at intermediate values of Oh. Hence, at intermediate values of Oh, the velocity has an appreciable rotational component

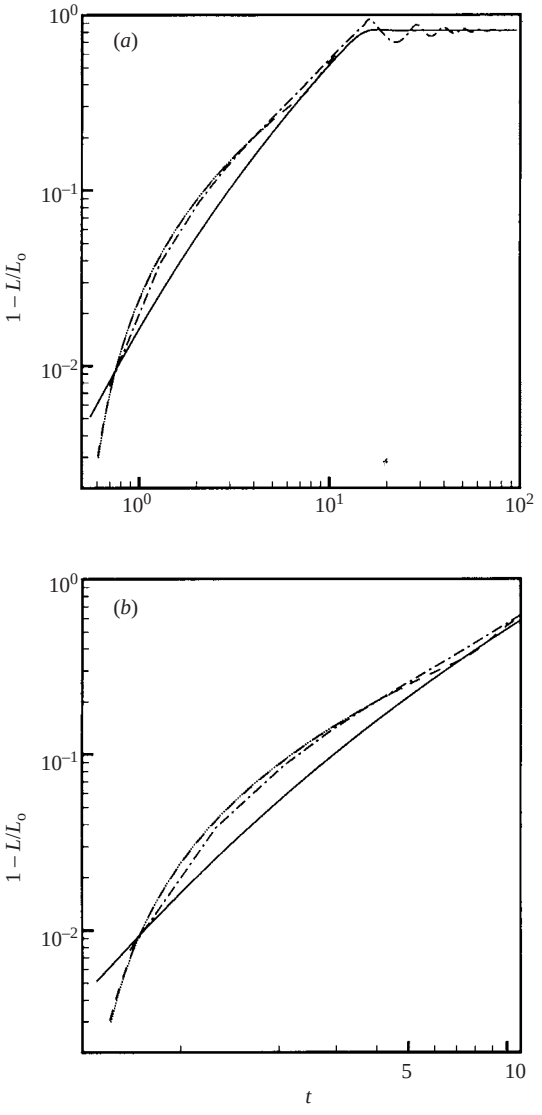

FIGURE 21. Variation of $1 - L/L_o$ with time t for filaments when $Oh = 1$ (solid line), 0.1 (chain-dashed line), 0.01 (dashed line), and 0.001 (dotted line). The initial aspect ratio $L_o = 15$ in all cases. (*a*) For all time and (*b*) for early times.

which the leading-order solution to the slender-jet equations cannot capture. This fact is further demonstrated by directly examining velocity fields and showing that recirculating flows do indeed exist within contracting filaments at intermediate values of Oh.

The computed prediction of the details of the pinch-off process has also been shown to agree with existing scaling theories of interface rupture. For sufficiently small values of Oh, a pinching interface initially evolves in time as if it enclosed an inviscid fluid. However, once the minimum radius becomes $O(Oh^2)$, the interface thereafter thins in accordance with the inertial-viscous scaling law.

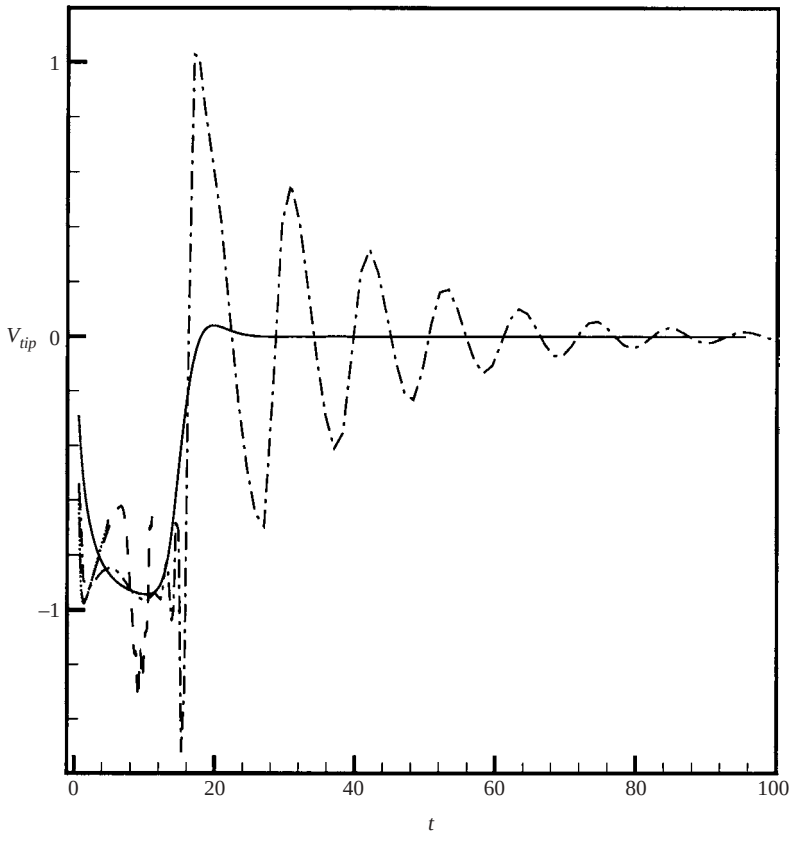

FIGURE 22. Variation of the tip velocity v_{tip} with time t for filaments when $Oh = 1$ (solid line), 0.1 (chain-dashed line), 0.01 (dashed line), and 0.001 (dotted line). The initial aspect ratio $L_o = 15$ in all cases.

This research was supported by the BES program of the US DOE. "Sandia is a multiprogram laboratory operated by Sandia Corporation, a Lockheed Martin Company for the United States Department of Energy's National Nuclear Security Administration under contract DE-AC04-94AL85000."

REFERENCES

AMBRAVANESWARAN, B. 2000 Deformation and breakup of drops and filaments. PhD thesis, Purdue University.

AMBRAVANESWARAN, B., PHILLIPS, S. D. & BASARAN, O. A. 2000 Theoretical analysis of a dripping faucet. *Phys. Rev. Lett.* **85**, 5332–5335.

AMBRAVANESWARAN, B., WILKES, E. D. & BASARAN, O. A. 2002 Drop formation from a capillary tube: Comparison of one-dimensional (1-d) and two-dimensional (2-d) analyses and occurence of satellite drops. *Phys. Fluids* **14**, 2606–2621.

BASARAN, O. A. 1992 Nonlinear oscillations of viscous liquid drops. *J. Fluid Mech.* **241**, 169–198.

BATHE, K.-J. 1982 *Finite Element Procedures in Engineering Analysis*. Prentice-Hall.

BECHTEL, S. E., CAO, J. Z. & FOREST, M. G. 1992 Practical application of a higher-order perturbation-theory for slender viscoelastic jets and fibers. *J. Non-Newtonian Fluid Mech.* **41**, 201–273.

BILLINGHAM, J. 1999 Surface-tension-driven flow in flat fluid wedges and cones. *J. Fluid Mech.* **397**, 45–71.

BRACKBILL, J. U. 1993 An adaptive grid with directional control. *J. Comput. Phys.* **108**, 38–50.

Brenan, K. E., Campbell, S. L. & Petzold, L. R. 1996 *Numerical Solution of Initial-Value Problems in Differential-Algebraic Equations*. Society for Industrial and Applied Mathematics.

Brenner, M. P., Eggers, J., Joseph, K., Nagel, S. R. & Shi, X. D. 1997 Breakdown of scaling in droplet fission at high Reynolds number. *Phys. Fluids* **9**, 1573–1590.

Chen, A. U. & Basaran, O. A. 2002 A new method for significantly reducing drop radius without reducing nozzle radius in drop-on-demand drop production. *Phys. Fluids* **14**, L1–L4.

Chen, A. U., Notz, P. K. & Basaran, O. A. 2002 Computational and experimental analysis of pinch-off and scaling. *Phys. Rev. Lett.* **88**, 4501–1–4501–4.

Chen, Y.-J. & Steen, P. H. 1997 Dynamics of inviscid capillary breakup: collapse and pinchoff of a film bridge. *J. Fluid Mech.* **341**, 245–267.

Christodoulou, K. N. & Scriven, L. E. 1992 Discretization of free surface flows and other moving boundary problems. *J. Comput. Phys.* **99**, 39–55.

Coyle, D. J. 1984 The fluid mechanics of roll coating: Steady flows, stability and rheology. PhD thesis, University of Minnesota.

Day, R. F., Hinch, E. J. & Lister, J. R. 1998 Self-similar capillary pinchoff of an inviscid fluid. *Phys. Rev. Lett.* **80**, 704–707.

Döring, M. 1982 Ink-jet printing. *Philips Tech. Rev.* **40**, 192–198.

Edgerton, H. E., Hauser, E. A. & Tucker, W. B. 1937 Studies in drop formation as revealed by the high-speed motion camera. *J. Phys. Chem.* **41**, 1017–1028.

Eggers, J. 1993 Universal pinching of 3d axisymmetric free-surface flow. *Phys. Rev. Lett.* **71**, 3458–3460.

Eggers, J. 1997 Nonlinear dynamics and breakup of free-surface flows. *Rev. Mod. Phys.* **69**, 865–929.

Eggers, J. 2000 Singularities in droplet pinching with vanishing viscosity. *SIAM J. Appl. Maths* **60**, 1997–2008.

Eggers, J. & Dupont, T. F. 1994 Drop formation in a one–dimensional approximation of the Navier-Stokes equation. *J. Fluid Mech.* **262**, 205–221.

Fuchikami, N., Ishioka, S. & Kiyono, K. 1999 Simulation of a dripping faucet. *J. Phys. Soc. Japan* **68**, 1185–1196.

Goedde, E. F. & Yuen, M. C. 1970 Experiments on liquid jet instability. *J. Fluid Mech.* **40**, 405–511.

Gresho, P. M., Lee, R. L. & Sani, R. L. 1980 On the time-dependent solution of the incompressible Navier-Stokes equations in two and three dimensions. In *Recent Advances in Numerical Methods in Fluids* (ed. C. Taylor & K. Morgan), vol. 1, chap. 2, pp. 27–79. Pineridge Press.

Gueyffier, D., Li, J., Nadim, A., Scardovelli, R. & Zaleski, S. 1999 Volume-of-fluid interface tracking with smoothed surface stress methods for three-dimensional flows. *J. Comput. Phys.* **152**, 423–456.

Hauser, E. A., Edgerton, H. E., Holt, B. M. & Cox Jr., J. T. 1936 The application of the high-speed motion picture camera to research on the surface tension of liquids. *J. Phys. Chem.* **40**, 973–988.

Henderson, D., Segur, H., Smolka, L. & Wadati, M. 2000 The motion of a falling liquid filament. *Phys. Fluids* **12**, 550–565.

Henderson, D. M., Pritchard, W. G. & Smolka, L. B. 1997 On the pinch–off of a pendant drop of viscous fluid. *Phys. Fluids* **9**, 3188–3200.

Hood, P. 1976 Frontal solution program for unsymmetric matrices. *Intl J. Numer. Meth. Engng* **10**, 379–399.

Hughes, T. J. R., Liu, W. K. & Zimmermann, T. K. 1981 Lagrangian-Eulerian finite element formulation for incompressible viscous flows. *Comput. Meth. Appl. Mech. Engng* **29**, 329–349.

Huyakorn, P. S., Taylor, C., Lee, R. L. & Gresho, P. M. 1978 Comparison of various mixed-interpolation finite-elements in velocity-pressure formulation of Navier-Stokes equations. *Comput. Fluids* **6**, 25–35.

James, A. J., Vukasinovic, B., Smith, M. K. & Glezer, A. 2003 Vibration-induced drop atomization and bursting. *J. Fluid Mech.* **476**, 1–28.

Keller, J. B. 1983 Breaking of liquid-films and threads. *Phys. Fluids* **26**, 3451–3453.

Keller, J. B., King, A. & Ting, L. 1995 Blob formation. *Phys. Fluids* **7**, 226–228.

Keller, J. B. & Miksis, M. J. 1983 Surface tension driven flows. *SIAM J. Appl. Math* **43**, 268–277.

Kheshgi, H. S. & Scriven, L. E. 1983 Penalty finite element analysis of unsteady free surface flows. In *Finite Elements in Fluids* (ed. R. H. Gallagher, J. T. Oden, O. C. Zienkiewicz, T. Kawai & M. Kawahara), vol. 5, p. 393. Wiley.

KISTLER, S. F. & SCRIVEN, L. E. 1983 Coating flows. In *Computational Analysis of Polymer Processing* (ed. J. R. A. Pearson & S. M. Richardson), chap. 8, pp. 243–299. Applied Science Publishers.

KISTLER, S. F. & SCRIVEN, L. E. 1994 The teapot effect: sheet-forming flows with deflection, wetting, and hysteresis. *J. Fluid Mech.* **263**, 19–62.

KNUPP, P. & STEINBERG, S. 1993 *Fundamentals of Grid Generation*. CRC Press.

KOWALEWSKI, T. A. 1996 On the separation of droplets from a liquid jet. *Fluid Dyn. Res.* **17**, 121–145.

LISTER, J. R. & STONE, H. A. 1998 Capillary breakup of a viscous thread surrounded by another viscous fluid. *Phys. Fluids* **10**, 2758–2764.

LUSKIN, M. & RANNACHER, R. 1982 On the smoothing property of the Galerkin method for parabolic equations. *SIAM J. Numer. Anal.* **19**, 93–113.

MANSOUR, N. N. & LUNDGREN, T. S. 1990 Satellite formation in capillary jet breakup. *Phys. Fluids* A **2**, 1141–1144.

NOTZ, P. K., CHEN, A. U. & BASARAN, O. A. 2001 Satellite drops: unexpected dynamics and change of scaling during pinch-off. *Phys. Fluids* **13**, 549–552.

PANTON, R. L. 1996 *Incompressible Flow*, 2nd edn. John Wiley & Sons.

PAPAGEORGIOU, D. T. 1995*a* Analytical description of the breakup of liquid jets. *J. Fluid Mech.* **301**, 109–132.

PAPAGEORGIOU, D. T. 1995*b* On the breakup of viscous liquid threads. *Phys. Fluids* **7**, 1529–1544.

PAPAGEORGIOU, D. T. & ORELLANA, O. 1998 Study of cylindrical jet breakup using one-dimensional approximations of the Euler equations. *SIAM J. Appl. Maths* **59**, 286–317.

PEREGRINE, D. H., SHOKER, G. & SYMON, A. 1990 The bifurcation of liquid bridges. *J. Fluid Mech.* **212**, 25–39.

ROBINSON, N. D. & STEEN, P. H. 2001 Observations of singularity formation during the capillary collapse and bubble pinch-off of a soap film bridge. *J. Colloid Interface Sci.* **241**, 448–458.

ROTHERT, A., RICHTER, R. & REHBERT, I. 2001 Transition from symmetric to asymmetric scaling function before drop pinch-off. *Phys. Rev. Lett.* **87**, 4501–1–4501–4.

RYSKIN, G. & LEAL, L. G. 1983 Orthogonal mapping. *J. Comput. Phys.* **50**, 71–100.

SACKINGER, P. A., SCHUNK, P. R. & RAO, R. R. 1996 A Newton-Raphson pseudo-solid domain mapping technique for free and moving boundary problems: a finite element implementation. *J. Comput. Phys.* **235**, 83–103.

SCHENA, M., HELLER, R. A., THERIAULT, T. P., KONRAD, K., LACHENMEIER, E. & DAVIS, R. W. 1998 Microarrays: biotechnology's discovery platform for functional genomics. *Trends Biotechnol.* **16**, 301–306.

SCHULKES, R. M. S. M. 1993 Nonlinear dynamics of liquid columns: A comparative study. *Phys. Fluids* A **5**, 2121–2030.

SCHULKES, R. M. S. M. 1994 The evolution and bifurcation of a pendant drop. *J. Fluid Mech.* **278**, 83–100.

SCHULKES, R. M. S. M. 1996 The contraction of liquid filaments. *J. Fluid Mech.* **309**, 277–300.

SHAH, P., KEVREKIDIS, Y. & BENZIGER, J. 1999 Ink-jet printing of catalyst patterns for electroless metal deposition. *Langmuir* **15**, 1584–1587.

SHI, X. D., BRENNER, M. P. & NAGEL, S. R. 1994 A cascade of structure in a drop falling from a faucet. *Science* **265**, 219–222.

SILLIMAN, W. J. 1979 Viscous film flows with contact lines. PhD thesis, University of Minnesota.

STONE, H. A., BENTLEY, B. J. & LEAL, L. G. 1986 An experimental study of transient effects in the breakup of viscous drops. *J. Fluid Mech.* **173**, 131–158.

STONE, H. A. & LEAL, L. G. 1989 Relaxation and breakup of an initially extended drop in an otherwise quiescent fluid. *J. Fluid Mech.* **198**, 399–427.

STRANG, G. & FIX, G. J. 1973 *An Analysis of the Finite Element Method*. Prentice-Hall.

TING, L. & KELLER, J. B. 1990 Slender jets and thin sheets with surface tension. *SIAM J. Appl. Maths* **50**, 1533–1546.

TJAHJADI, M., STONE, H. A. & OTTINO, J. M. 1992 Satellite and subsatellite formation in capillary breakup. *J. Fluid Mech.* **243**, 297–317.

WALTERS, R. A. 1980 The frontal method in hydrodynamics simulations. *Comput. Fluids* **8**, 265–272.

WILKES, E. D. 1999 Nonlinear dynamics of oscillations and breakup of supported drops. PhD thesis, Purdue University.

Wilkes, E. D. & Basaran, O. A. 2001 Drop ejection from an oscillating rod. *J. Colloid Interface Sci.* **242**, 180–201.

Wilkes, E. D., Phillips, S. D. & Basaran, O. A. 1999 Computational and experimental analysis of dynamics of drop formation. *Phys. Fluids* **11**, 3577–3598.

Zhang, D. F. & Stone, H. A. 1997 Drop formation in viscous flows at a vertical capillary tube. *Phys. Fluids* **9**, 2234–2242.

Zhang, X. 1999 Dynamics of growth and breakup of viscous pendant drops into air. *J. Colloid Interface Sci.* **212**, 107–122.

Zhang, X. & Basaran, O. A. 1995 An experimental study of dynamics of drop formation. *Phys. Fluids* **7**, 1184–1203.